Molecular evidence of anteroposterior patterning in adult echinoderms

Formery, L.[1,2,*], Peluso, P.[3], Kohnle, I.[1], Malnick, J.[1], Thompson, J. R.[4,5], Pitel, M.[6], Uhlinger, K. R.[1], Rokhsar, D. S.[2,7,8,+], Rank, D. R.[3,+], Lowe, C. J.[1,7,+,*]

1: Department of Biology, Hopkins Marine Station, Stanford University, Pacific Grove, CA, USA

2: Department of Molecular and Cell Biology, University of California Berkeley, Berkeley, CA, USA

3: Pacific Biosciences, Menlo Park, CA, USA

4: School of Biological Sciences, University of Southampton, Southampton, UK

5: School of Ocean and Earth Science, University of Southampton, Southampton, UK

6: Columbia Equine Hospital, Gresham, OR, USA

7: Chan Zuckerberg BioHub, San Francisco, CA, USA

8: Molecular Genetics Unit, Okinawa Institute of Science and Technology, Onna, Okinawa, Japan

+: These authors contributed equally to this work

*: Corresponding authors: Laurent Formery, 120 Oceanview Blvd, Pacific Grove, 93950 CA, USA (email address: laurent.formery@gmail.com); Christopher Lowe, 120 Oceanview Blvd, Pacific Grove, 93950 CA, USA (email address: clowe@stanford.edu)

Keywords: Echinoderms, Axial patterning, Body plan evolution, Pentaradial symmetry, RNA tomography

Authors ORCID IDs:

Laurent Formery https://orcid.org/0000-0003-0230-4051
Paul Peluso https://orcid.org/0000-0002-9723-5185
Jeffrey R. Thompson https://orcid.org/0000-0003-3485-172X
Mariya Pitel https://orcid.org/0000-0002-3321-2136
Daniel S. Rokhsar https://orcid.org/0000-0002-8704-2224
David R. Rank https://orcid.org/0000-0001-9213-6965
Christopher J. Lowe https://orcid.org/0000-0002-7789-8643

Abstract

The origin of the pentaradial body plan of echinoderms from a bilateral ancestor is one of the most enduring zoological puzzles[1,2]. Since echinoderms are defined by morphological novelty, even the most basic axial comparisons with their bilaterian relatives are problematic. To revisit this classical question, we used conserved antero-posterior (AP) axial molecular markers to determine whether the highly derived adult body plan of echinoderms masks underlying patterning similarities with other deuterostomes. We investigated the expression of a suite of conserved transcription factors with well-established roles in the establishment of AP polarity in deuterostomes[3-5] and other bilaterians[6-8] using RNA tomography and *in situ* hybridization in the sea star *Patiria miniata*. The relative spatial expression of these markers in *P. miniata* ambulacral ectoderm shows similarity with other deuterostomes, with the midline of each ray representing the most anterior territory and the most lateral parts exhibiting a more posterior identity. Strikingly, there is no ectodermal territory in the sea star that expresses the characteristic bilaterian trunk genetic patterning program. This suggests that from the perspective of ectoderm patterning, echinoderms are mostly head-like animals, and provides a developmental rationale for the reevaluation of the events that led to the evolution of the derived adult body plan of echinoderms.

Introduction

Echinoderms, defined by their calcitic endoskeleton, unique water vascular system, and perhaps most strikingly by their pentaradial body plan[1,2], are among the most enigmatic animal phyla. Since echinoderms are phylogenetically nested within the deuterostomes[9,10] (echinoderms, hemichordates, and chordates), their pentaradial organization was evidently derived from a bilateral ancestor. Yet, despite a rich fossil record, comparative morphological studies have come to conflicting conclusions regarding the axial transformations that led to pentamery from the ancestral bilaterian state[2,11]. Among bilaterians, the deployment of the gene regulatory network that specifies ectoderm AP polarity is highly conserved[3-8] and represents a suite of characters that is often more conserved than the body plans they regulate[4,5] (Fig. 1a). The deployment of this AP gene regulatory network could therefore provide an alternative way to test hypotheses of axial homology in cases such as echinoderms where morphological characters are too divergent to reconstruct ancestral states[12].

Detailed comparisons between chordate and hemichordate axial patterning have established the exquisite conservation of the deuterostome ectodermal AP patterning program[4,5], which provides a phylogenetically robust framework for addressing the evolution of echinoderm axial properties. We considered two contrasting scenarios. First, the ancestral deuterostome AP patterning network could have been dismantled and reassembled into novel conformations during the radical body plan modifications along the echinoderm stem lineage. In this scenario, expression of transcription factors in derived morphological structures without extensive conservation of relative spatial expression would imply co-option into novel developmental roles[13,14]. Alternatively, conservation of spatially coordinated expression of this network during the elaboration of the echinoderm adult body plan would provide a molecular basis for testing hypotheses of axial homology with bilaterians, and establish regional homologies masked by divergent anatomies[12] (Fig. 1b).

Under the second scenario, four main hypotheses have been proposed to relate the echinoderm body plan to other bilaterians that explicitly consider axial homology (Fig.1c). The bifurcation[15] and the circularization[15,16] hypotheses can be ruled out, since they require a unique molecular identity for each of the five echinoderm rays that is inconsistent with molecular data[17]. In the duplication hypothesis[15,18], each of the five echinoderm rays is a copy of the ancestral AP axis joined anteriorly in the disk, and in the stacking hypothesis[2,11,19] the oral-aboral axis of adult echinoderms is homologous to the ancestral AP axis. Although broad bilaterian comparisons of AP axis patterning are typically based on ectodermal expression domains, the stacking hypothesis was proposed largely on the basis of nested posterior Hox gene expression in the posterior mesoderm of the bilateral larval stages in holothuroids (sea cucumbers), crinoids (sea lilies), and echinoids (sea urchins)[20-26]. While initially restricted to coelomic compartments[2,19], some iterations of the stacking hypothesis have also included the oral ectoderm as the

most anterior compartment[11]. However, recent analyses suggest that the anterior identity of the oral ectoderm should be considered independent of mesoderm derivatives[27].

Here, we tested these classical hypotheses by examining gene expression in the asteroid (sea star) *Patiria miniata* (Extended Data Fig. 1a,b), using a statistical approach based on spatial transcriptomics and *in situ* hybridization. Our data provide evidence for unexpected conservation of the ancestral AP ectodermal patterning network during ambulacrum development in juveniles. Importantly, our results do not fit with any of the established hypotheses and instead suggest a new ambulacral-anterior model to relate echinoderm pentaradial symmetry to the ancestral bilateral symmetry.

Results and discussion

RNA tomography in adult *Patiria miniata*

The manifestation of pentaradial symmetry in asteroids is simpler than in other echinoderm classes because it follows a planar organization with the rays extending around the oral-aboral axis through easily distinguishable alternating ambulacral territories (where the grooves bearing the tube feet are located) and interradial territories (Fig. 2a). This makes asteroids particularly well-suited for investigating potential axial homologies between the pentaradial echinoderm body plan and closely related bilateral deuterostomes using the molecular anatomy coordinates offered by the conserved, ectodermal AP patterning network. The adult body plan of asteroids is defined by the endoskeleton, which underlies the body wall in the aboral and interradial areas, the digestive tract and pyloric caeca, the main body muscles, the water vascular system along each ambulacrum, and the central nervous system that includes five radial nerve cords and the circumoral nerve ring. We used micro computed tomography (micro-CT) to show the exact spatial arrangement of the principal anatomical features in *P. miniata* juveniles along each organizational plane of the juvenile arms (Fig. 2a, Extended Data Fig. 1c,d; Supplementary Fig. 1; Supplementary Video 1).

Within this anatomical framework, we began investigating the transcriptional landscape of *P. miniata* along its body axes with an unbiased spatial transcriptomics approach using RNA tomography[28]. We cryo-sectioned three arms from *P. miniata* juveniles at a stage that matched the micro-CT scanned specimen, along three different dimensions: from the proximal to the distal part of the arm (P-D), from the oral to the aboral side (O-A), and from the left to the right side (hereafter referred to as medio-lateral; M-L) (Fig. 2b; Extended Data Fig. 1c, Supplementary Video 1; Supplementary Fig. 2a-c). Sections were barcoded and pooled for single molecule real time sequencing with PacBio IsoSeq (Supplementary Fig. 2d,e; Supplementary Fig. 3a-d; Supplementary Tables 1-4), yielding a three-dimensional atlas of 25,794 gene expression profiles along the P-D, O-A and M-L dimensions of *P. miniata* arms (Fig. 2c). Gene clustering based on the similarity of RNA tomography expression profiles highlighted seven principal patterns of gene expression (Fig. 2c). We confirmed that transcriptional landscape determined by RNA tomography was consistent with the anatomy of the animal by considering principal component analyses and Spearman correlations between sections along each dimension and analyzing the expression profile of marker genes known to be expressed in specific tissues (Extended Data Fig. 1e-g). To aid in this analysis we generated a new *P. miniata* genome assembly (Supplementary Fig. 2e; Supplementary Fig. 3d,e; Supplementary Tables 4,5).

To consider possible molecular anatomical homologies across deuterostomes we identified 36 conserved molecular markers in the RNA tomography dataset that define specific ectoderm territories along the AP axis in hemichordates and chordates (Fig. 1a; Supplementary Fig. 4) and retrieved their expression profiles (Fig. 2d). These marker genes included transcription factors (*fezF*, *six3/6*, *nkx2.1*, *foxG*, *lhx2/9*, *otp*, *dmbx*, *tlx*, *emx*, *barH1*, *pax6*, *irx*, *dbx*, *otx*, *lhx1/5*, *engrailed*, *gbx*, *pax2/5/8*, *hox1*, *hox2*, *hox3*, *hox4*, *hox5*, *hox7*, *hox8*, *hox9/10*, *hox11/13b*); members of the Wnt signaling pathway (*sfrp1/5*, *sfrp3/4*, *fzd5/8*, *wnt3*); and the ligand *hedgehog*. Four additional transcription factor markers (*rx*, *dlx*, *hox11/13a* and *hox11/13c*) were excluded from the computational analyses because of low expression levels (Supplementary Fig. 3f). *Hox6* was absent in our Hox cluster assembly (Supplementary Fig. 5), as

reported previously in the closely related species *P. pectinifera*[29] and in the crown of thorns sea star *Acanthaster planci*[30], consistent with its loss in valvatid asteroids.

The duplication and stacking hypotheses would be supported by staggered expression of these AP patterning markers along the P-D or O-A dimensions, respectively. We ranked the AP patterning markers from the anterior to posterior using the hemichordate *Saccoglossus kowalevskii* as a template, since it is the most closely related bilateral species with a comprehensive expression pattern dataset for these markers (Supplementary Fig. 6). We then tested the Spearman correlation between the ranking of the genes and their position along the P-D and O-A dimensions. In both cases, we found moderate but not statistically significant correlations (ρ=0.25, p=0.16 and ρ=0.27, p=0.13, respectively) (Fig. 2e). Organizing the AP patterning genes into seven groups based on their expression profiles (Supplementary Fig. 6b), we found that the moderate correlation with the O-A dimension was mostly explained by the Hox genes alone (Fig. 2f). This was expected, since the stacking hypothesis was primarily informed by the sequential expression of Hox genes in mesoderm derivatives[11,19].

Unexpectedly, we found a much stronger correlation (ρ=0.62, p=1.4×10^{-4}) between gene order and the medio-lateral axis (M-L) (Fig. 2e). The most anterior genes appeared to be largely expressed close to the midline of the arm, while more posterior genes were expressed more laterally on either side of the midline. To confirm that the observed correlations were robust and not the result of sensitivity to the AP patterning gene ranking assigned from the *in situ* hybridization expression data, we simultaneously shuffled the gene ranking within each of the 7 groups and probabilistically sampled the position for each gene, using the expression z-score as a law of probability, over 10^6 replications. For all the simulated replications, the distribution of M-L correlations was significantly superior to the P-D and O-A correlations, with a two-sided Wilcoxon-rank test p-value inferior to 10^{-4} in both cases (Fig. 2e). This suggests that neither the duplication nor the stacking hypotheses accurately describe the deployment of AP-related patterning genes in *P. miniata*, and that most of the underlying patterning logic of the pentaradial plan is not explained by existing models.

M-L deployment of AP patterning genes

While RNA tomography provides coarse average axial positional information, these patterns cannot be directly linked to germ layers or anatomical structures. To investigate axial patterning in more detail, we examined the expression pattern of the 36 marker genes using *in situ* hybridization chain reactions (HCR, Supplementary Fig. 7) on post-metamorphic juveniles. This representative stage follows the resorption of larval structures into the rudiment during metamorphosis (Fig. 3a). The elaboration of the pentaradial symmetry is initiated earlier within the larval mesoderm, but the mechanistic basis of this process is likely distinct from those that give their regional identity to the final axes of the pentaradial body plan. Classical ectoderm AP patterning genes such as *six3/6*, *nkx2.1*, *dmbx*, *pax6* and *otx* initiated expression at low levels in the presumptive adult tissues at the onset of metamorphosis, but only reached robust levels of expression that were relatable to ambulacral polarity in post-metamorphic juveniles, when the definitive adult body plan is elaborated (Fig. 3b; Supplementary Fig. 8). We focused on early juvenile stages as a readout of early establishment of axial patterning. As in the adult, the juvenile body plan is organized into ambulacral territories on the oral side and interradial territories at the edge of the ambulacra and extending around to envelope the entire aboral side. The ambulacral ectoderm is divided in two main regions: the medial ambulacral ectoderm comprising the radial nerve cords (RNCs) and the circumoral nerve ring (CNR), and more laterally the epidermis covering the podia (Fig. 3c,d).

We analyzed the expression of four groups of patterning genes expressed along the AP axis in both hemichordates and chordates. The first group (*fzd5/8*, *nkx2.1*, *rx*, *sfrp1/5, foxG*, *six3/6, hedgehog*) has strong anterior ectodermal localizations in the proboscis of *S. kowalevskii*[4,5] and in the forebrain of vertebrates[31,32] (Fig. 1a,b). In *P. miniata* we found similarly overlapping patterns of regional expression, mostly restricted to the developing CNR, the RNCs, and in the case of *six3/6* and *hedgehog,* in repeated domains where lateral nerves from the RNCs connect with each pair of secondary podia (Fig. 3e-l; Supplementary Fig. 9a-e). This region corresponded to the most medial part of the ambulacral ectoderm

(Fig. 3d). These findings are inconsistent with the duplication hypothesis, which predicts a staggered expression of anterior to posterior markers along each RNC.

The next group (*lhx1/5*, *dmbx*, *tlx, irx*, *fezF*, *dbx*, *otx*, *barH* and *pax6)* overlaps with the previous anterior-class genes in *S. kowalevskii* but with a more caudal distribution in the posterior proboscis and into the collar[4]; in chordates, these genes are primarily expressed either in the forebrain or the midbrain[3,31] (Fig. 1a,b). In *P. miniata*, expression of this group of genes overlaps in the most medial territory with the most anterior class genes, but with expanded lateral domains on either side of the RNCs (Fig. 3d, m-s; Supplementary Fig. 9f-h), into the epidermis covering the podia. *FezF* and *dbx* were only expressed in a limited number of cells in the ambulacral ectoderm (Supplementary Fig. 10a-c). Only *pax6* was not expressed in the medial ambulacral ectoderm and was restricted to the podia epidermis, as previously reported in other echinoderm species[33,34] (Fig. 3t). Thus, the lateral ambulacral ectoderm appears to have a more posterior molecular identity, similar to that of the hemichordate collar or the vertebrate midbrain.

The third category (*gbx*, *wnt3*, *hox1*, *pax2/5/8*) includes genes that have more posterior expression patterns in hemichordates and chordates (Fig. 1a,b). *Gbx*, *hox1* and *pax2/5/8* are all expressed in hemichordates in the anterior trunk, close to the boundary with the collar, and in chordates in the hindbrain and into the midbrain/hindbrain boundary[5,35,36]. *Wnt3* is expressed at the far posterior end of the AP axis in both phyla[37,38]. In *P. miniata*, we found that these four genes are expressed at the boundary between the ambulacral ectoderm and the interradial territory (Fig. 3d, u-β; Supplementary Fig. 9i-l). *Gbx* and *wnt3* were expressed in the outer part of the ambulacral ectoderm, establishing a mutually exclusive boundary with more anterior genes like *six3/6* (Fig. 3u-x). *Hox1* and *pax2/5/8* were expressed more laterally compared to *gbx* and *wnt3*: *hox1* outlined the entire ambulacral area, while *pax2/5/8* had a more complex expression pattern and was primarily expressed between the ambulacra (Fig. 3y-β). We suggest that in *P. miniata* these genes marked the outer limit of an anterior compartment.

Finally, Hox genes are expressed in hemichordates and chordates posteriorly to the collar/trunk and midbrain/hindbrain boundary, respectively, and are involved in trunk patterning[4,35,39] (Fig. 1a,b). In *P. miniata*, only *hox1* was detected in the ectoderm. *Hox3*, *hox5*, *hox8* and *hox9/10* were expressed in mesoderm derivatives (Fig. 3γ-ζ). *Hox4* expression was barely above the detection threshold but was found in the pharynx (Fig. 3η), while *hox7*, *hox11/13a* and *hox11/13b* were expressed in the developing intestinal tract (Fig. 3θ-κ). These observations are in line with previous reports that Hox expression in echinoderms is largely restricted to internal germ layers[20-26] and consistent with the Hox-driven O-A correlation observed in our RNA tomography dataset. In hemichordates and other bilaterians, Hox gene domains are intercalated during trunk development between the anterior domains and the posterior end of the animal, which expresses posteriorizing factors such as *wnt3*[35,40]. We propose that there is no ectoderm equivalent to a trunk region in *P. miniata*, because *wnt3* is expressed at the edge of the ambulacral region, and because *hox1* is the only Hox gene expressed in the ectoderm. Therefore, the deployment of the AP patterning system in *P. miniata* seems to be limited to the ambulacral region and its boundary.

We also found that in *P. miniata* some ancestral deuterostome AP patterning genes did not exhibit conserved relative expression relative to hemichordates and vertebrates, either because they were not detected (*dlx*), not expressed in the ectoderm (*engrailed*, *sfrp3/4*), or exhibited different relative spatial arrangements (*lhx2/9*, *emx*, *otp*) (Supplementary Fig. 10d-i). Some well-established boundaries in hemichordates and vertebrates like the abutting *otx* and *gbx* domains were also not observed in *P. miniata*. This presumably reflects the plasticity of the AP patterning system and its adaptation to the radically different pentaradial body plan. Despite these discrepancies, germ-layer specific expression patterns corroborate that the M-L dimension revealed by RNA tomography, is the main and unexpected driver of the ectoderm AP patterning logic of the pentaradial body plan in *P. miniata*.

If the ancestral deuterostome AP patterning system is used to remodel the sea star body plan at metamorphosis, are other correlated bilaterian axial patterning systems contributing to the patterning of the adult body plan as well? In bilaterians, the dorso-ventral (DV) axis is specified transiently during embryogenesis by conserved BMP2/4 and Chordin gradients[41,42]. Later on, the neuroectoderm and

mesoderm derivatives are patterned along the DV axis via the deployment of transcription factors such as *pax3/7*, *msx* and *tbx2/3* in response to BMP signaling[43-45] (Extended Data Fig. 2a). To investigate whether the BMP/Chordin axis is involved in the formation of the adult body plan in *P. miniata*, we first looked at the expression of genes involved in DV axis specification through metamorphosis and in post-metamorphic juveniles (Extended Data Fig. 2b-s; Supplementary Fig. 4). While *chordin* was not detected by *in situ* hybridization, we found that *BMP2/4*, *BMP1* and *ADMP1* were consistently expressed in the distal part of the developing tube feet mesoderm, starting early in metamorphosis and into the juvenile (Extended Data Fig. 2c-s). In addition, we looked at known target genes of BMP signaling (Extended Data Fig. 2b,t-v; Supplementary Fig. 4). While *pax3/7* is lost in echinoderms[46], *tbx2/3* and *msx* were co-expressed with *BMP2/4* in the tube feet, and *tbx2/3* also expressed in the overlying tube feet ectoderm, suggesting a similar relationship to BMP signaling than in vertebrates (Extended Data Fig. 2t-v). These expression data are consistent with previous studies from a direct-developing echinoid[47] and support a role for BMP signaling in tube feet development, more equivalent to the later patterning role of BMP in dorsal midline patterning in hemichordates and vertebrates[43,48]. However, our results do not indicate BMP/Chordin signaling as defining an anatomical axis in the pentaradial body plan of *P. miniata*.

Echinoderm rays have also been proposed to be homologous to bilaterian appendages[49,50]. In principle, this scenario could be compatible with our expression data, with the rays being appendages of an anterior territory. To assess this possibility, we considered conserved markers for proximo-distal appendage development, which involves polarized expression of *meis*, *pbx*, *dlx* and *sp8-9* in vertebrates, arthropods and cephalopods[51] (Extended Data Fig. 2w,x; Supplementary Fig. 4). Although we found the expression of *Pbx* and particularly *sp8-9* to be compatible with this idea, *dlx* was not detected and *meis* had an inconsistent expression domain (Extended Data Fig. 2x-α). The extension of the echinoderm ambulacra likely involves substantial developmental novelty. The RNA tomography dataset will be an invaluable resource for hypothesis generation and identification of candidate genes to form the basis of a more in depth developmental investigations of this process.

Evolution of axial properties in echinoderms

The organizational modifications to the ancestral bilateral deuterostome body plan during early echinoderm evolution are so profound that even basic axial comparisons with other deuterostome taxa have been problematic at the morphological level[2]. Here we investigated this fundamental question by spatially mapping the deployment of the ancestral bilaterian ectodermal AP patterning system in the pentaradial body plan of *P. miniata*. Since this patterning system is largely conserved between hemichordates and chordates, we can confidently reconstruct its ancestry in early deuterostomes and at the base of ambulacrarians[4,5].

We found that that much of the ancestral anterior patterning network is spatially deployed in a manner incompatible with previously proposed hypotheses of echinoderm axial homologies[11,15]. Rather, expression patterns map onto a novel coordinate system that we call the "ambulacral-anterior" model of echinoderm body plan evolution (Fig. 4a,b). In this model, the midline of each ambulacrum expresses the most anterior bilaterian molecular identity, equivalent to the forebrain and proboscis in vertebrates and hemichordates, respectively. The mid-lateral regions on either side of the nerve cords, including the ectoderm wrapping the podia, share patterning similarities with more caudal ectodermal territories of hemichordates and chordates, down to the collar and midbrain, respectively. Finally, the boundary at the edge of the ambulacral ectoderm displays the most posterior molecular profile corresponding to the collar/trunk boundary of hemichordates and the midbrain/hindbrain boundary of vertebrates. According to our ambulacral-anterior model, echinoderms are the first example of bilaterians in which the "anterior" identity is located at the center of a sheet of tissue, rather than being located at an extremity. The anatomical outputs of this anterior domain, however, share similarities across all deuterostome phyla (including echinoderms) in that they include neural condensations and an extensive array of sensory structures.

Strikingly, despite the presence of a genomic Hox cluster, ectodermal Hox gene expression is largely absent in the sea star (except for *hox1*), suggesting a loss of the ancestral ectodermal trunk regulatory program, which is consistent with previous observations in the echinoid *Peronella japonica*[27]. Yet, Hox genes are expressed in the mesoderm and endoderm, displaying a marked uncoupling of germ layer AP patterning as recognized previously[27,52]. The mesoderm and endoderm trunk programs are wrapped in an ectoderm with two clear territories, including (1) an ambulacral anterior-like domain that is the main focus of our work, and unexpectedly (2) an extensive interradial domain that extends around the aboral side of the animal and displays uncertain axial identity, without any detectable readout of the ancestral AP patterning program, as previously observed in echinoids[27]. The uncoupling of an ectodermal head and trunk programs is not unique to *P. miniata* and has been demonstrated in both larval echinoderms and hemichordates[35,53], and more recently in protostome larvae[40,54], suggesting that these regulatory programs can be uncoupled over macro-evolutionary time frames.

Previous studies[13,14] proposed that the deployment of transcription factors to pattern adult echinoderm body plans could be the result of co-option, meaning recruitment of an existing gene or regulatory module (or duplication thereof) to fulfill a new developmental role[55]. Here, using a much larger set of genes, we demonstrate that the patterning of the ambulacral ectoderm in *P. miniata* involves a collection of interacting modules that define distinct regions along the AP axis of bilateral animals rather than a single regulatory program. Cooption of this network would require redeployment of these interacting modules into a novel role in stem echinoderms. Thus, while we acknowledge that co-option remains a possible scenario, we propose that the observed pattern in extant asteroid ambulacra is a result of modification of an ancestral deuterostome axial program during echinoderm evolution. Documented cases of co-option such as the deployment of posterior Hox genes during limb patterning[56] involve the (re)use of an existing regulatory network to pattern a new structure, without affecting the ancestral role of the system. To our knowledge there is no example of co-option that involves dismantling of the ancestral patterning networks following their recruitment into the development of a novel structure. A co-option scenario in echinoderms would imply that the ancestral function of the AP patterning network was lost in the adult body plan, after co-option into an evolving ambulacral territory, which in our opinion is less parsimonious than proposing descent with modification of an ancestral AP axis. Interestingly, a route to resolve this issue might come from some interpretations of homalozoan and helicoplacoid echinoderms that propose these groups to be transitional forms between bilateral and pentaradial symmetry[57]. Re-interpreting these fossils in light of new patterning datasets could allow us to discriminate between co-option with loss of the ancestral axial registry, or descent with modification.

Did the reorganization of the ancestral AP axis documented here occur during the early stem evolution of echinoderms as a defining regulatory feature of crown group echinoderms, or during the later diversification of asteroids? Our model inferred from analysis of asteroid data is consistent with published findings from two other major echinoderm clades, crinoids and echinoids. In crinoids, the expression of *six3/6*, *otx,* and *pax6* has been reported in the ambulacral ectoderm[58]. In echinoids, AP patterning related genes have been surveyed in various species including *Strongylocentrotus purpuratus* and *Heliocidaris erythrogramma*[20,33,34], and most extensively in *Peronella japonica*[25,27] where the anterior identity of the ambulacral ectoderm was already reported[27]. In both crinoids and echinoids, most of the anterior patterning related genes studied show expression patterns compatible with the ambulacral-anterior model. Furthermore, Hox gene expression has been described in echinoids, holothuroids, and crinoids[20-26] and is also largely congruent with the expression patterns that we observed in *P. miniata*. This suggests that based on limited available comparative data, the ambulacral-anterior model could be a general development feature of all extant echinoderm classes and that our observations reflect early regulatory changes that occurred during stem echinoderm evolution (Fig.4c). Further comprehensive comparative analyses will be required to test this hypothesis.

The evolution of body plan variations across echinoderm classes has proven challenging to reconstruct based on morphological features alone[59]. The ambulacral-anterior model offers a powerful tool to establish robust regional homologies between echinoderm classes. Most importantly, the new axial paradigm established here can be integrated with the exquisite fossil record of the phylum to reinvestigate key morphological transformations in light of regulatory changes.

References

1. Hyman, L. H. The Invertebrates, Vol. IV, Echinodermata: The coelomate Bilateria. (McGraw-Hill, 1955).
2. Smith, A. B. Deuterostomes in a twist: the origins of a radical new body plan. *Evol. Dev.* **10**, 493-503 (2008).
3. Albuixech-Crespo, B. *et al*. Molecular regionalization of the developing amphioxus neural tube challenges major partitions of the vertebrate brain. *PLoS Biol.* **15**, e2001573 (2017).
4. Lowe, C. J. *et al*. Anteroposterior patterning in hemichordates and the origins of the chordate nervous system. *Cell* **113**, 853-865 (2003).
5. Pani, A. M., Mullarkey, E. E., Aronowicz, J., Assimacopoulos, S., Grove, E. A., & Lowe, C. J. Ancient deuterostome origins of vertebrate brain signalling centres. *Nature* **483**, 289-294 (2012).
6. Reichert, H., & Simeone, A. Developmental genetic evidence for a monophyletic origin of the bilaterian brain. *Philos. Trans. R. Soc. Lond., B, Biol. Sci.* **356**, 1533-1544 (2001).
7. Hirth, F., Kammermeier, L., Frei, E., Walldorf, U., Noll, M., & Reichert, H. An urbilaterian origin of the tripartite brain: developmental genetic insights from Drosophila. *Development* **130**, 2365–2373 (2003).
8. Tomer, R., Denes, A. S., Tessmar-Raible, K., & Arendt, D. Profiling by image registration reveals common origin of annelid mushroom bodies and vertebrate pallium. *Cell* **142**, 800-809 (2010).
9. Bromham, L. D., & Degnan, B. M. Hemichordates and deuterostome evolution: robust molecular phylogenetic support for a hemichordate+echinoderm clade. *Evol. Dev.* **1**, 166-171 (1999).
10. Cameron, C. B., Garey, J. R., & Swalla, B. J. Evolution of the chordate body plan: new insights from phylogenetic analyses of deuterostome phyla. *PNAS* **97**, 4469-4474 (2000).
11. David, B., & Mooi, R. How Hox genes can shed light on the place of echinoderms among the deuterostomes. *EvoDevo* **5**, 1-19 (2014).
12. Lowe, C. J., Clarke, D. N., Medeiros, D. M., Rokhsar, D. S., & Gerhart, J. The deuterostome context of chordate origins. *Nature* **520**, 456-465 (2015).
13. Lowe, C. J., & Wray, G. A. Radical alterations in the roles of homeobox genes during echinoderm evolution. *Nature* **389**, 718-721 (1997).
14. Li, Y., *et al.* (2020). Genomic insights of body plan transitions from bilateral to pentameral symmetry in Echinoderms. *Com. Biol* **3**, 1-10.
15. Popodi, E., Andrews, M., & Raff, R. A. Evolution of body plans: using homeobox genes to examine the development of the radial CNS of echinoderms. *Dev. Biol.* **163**, 540 (1994).
16. Rozhnov, S. V. Symmetry of echinoderms: from initial bilaterally-asymmetric metamerism to pentaradiality. *Nat. Sci.* **6**, 171-183 (2014).
17. Holland, L. Z. Evolution of basal deuterostome nervous systems. *J. Exp. Biol.* **218**, 637-645 (2015).
18. Byrne, M., Martinez, P., & Morris, V. Evolution of a pentameral body plan was not linked to translocation of anterior Hox genes: the echinoderm HOX cluster revisited. *Evol. Dev.* **18**, 137-14 (2016).
19. Peterson, K. J., Arenas-Mena, C., & Davidson, E. H. The A/P axis in echinoderm ontogeny and evolution: evidence from fossils and molecules. *Evol. Dev.* **2**, 93-101 (2000).
20. Arenas-Mena, C., Cameron, A. R., & Davidson, E. H. Spatial expression of Hox cluster genes in the ontogeny of a sea urchin. *Development* **127**, 4631-4643 (2000).
21. Morris, V. B., & Byrne, M. Involvement of two Hox genes and Otx in echinoderm body-plan morphogenesis in the sea urchin *Holopneustes purpurescens*. *J. Exp. Zool. B Mol.* **304**, 456-467 (2005).
22. Hara, Y., Yamaguchi, M., Akasaka, K., Nakano, H., Nonaka, M., & Amemiya, S. Expression patterns of Hox genes in larvae of the sea lily *Metacrinus rotundus*. *Dev. Genes Evol.* **216**, 797-809 (2006).
23. Cisternas, P., & Byrne, M. Expression of Hox4 during development of the pentamerous juvenile sea star, *Parvulastra exigua*. *Dev. Genes Evol.* **219**, 613-618 (2009).
24. Morris, V. B., & Byrne, M. Oral–aboral identity displayed in the expression of HpHox3 and HpHox11/13 in the adult rudiment of the sea urchin *Holopneustes purpurescens*. *Dev. Genes Evol.* **224**, 1-11 (2014).

25. Tsuchimoto, J., & Yamaguchi, M. Hox expression in the direct-type developing sand dollar *Peronella japonica*. *Dev. Dyn.* **243**, 1020-1029 (2014).
26. Kikuchi, M., Omori, A., Kurokawa, D., & Akasaka, K. Patterning of anteroposterior body axis displayed in the expression of Hox genes in sea cucumber *Apostichopus japonicus*. *Dev. Genes Evol.* **225**, 275-286 (2015).
27. Adachi, S. *et al*. Anteroposterior molecular registries in ectoderm of the echinus rudiment. *Dev. Dyn.* **247**, 1297-1307 (2018)
28. Junker, J. P. *et al*. Genome-wide RNA tomography in the zebrafish embryo. *Cell* **159**, 662-675 (2014).
29. Tominaga, H., Nishitsuji, K., & Satoh, N. A single-cell RNA-seq analysis of early larval cell-types of the starfish, *Patiria pectinifera*: Insights into evolution of the chordate body plan. *Dev Biol*. **496**, 52-62. (2023).
30. Baughman, K. W., McDougall, C., Cummins, S. F., Hall, M., Degnan, B. M., Satoh, N., & Shoguchi, E. Genomic organization of Hox and Para Hox clusters in the echinoderm, *Acanthaster planci*. *Genesis* **52**, 952-958 (2014).
31. Shimamura, K., Hartigan, D. J., Martinez, S., Puelles, L., & Rubenstein, J. L. Longitudinal organization of the anterior neural plate and neural tube. *Development* **121**, 3923-3933 (1995).
32. Quinlan, R., Graf, M., Mason, I., Lumsden, A., & Kiecker, C. Complex and dynamic patterns of Wnt pathway gene expression in the developing chick forebrain. *Neural development* **4**, 1-27 (2009).
33. Byrne, M., Koop, D., Morris, V. B., Chui, J., Wray, G. A., & Cisternas, P. Expression of genes and proteins of the pax-six-eya-dach network in the metamorphic sea urchin: Insights into development of the enigmatic echinoderm body plan and sensory structures. *Dev. Dyn.* **247**, 239-249 (2018).
34. Paganos, P., *et al*. New Model Organism to Investigate Extraocular Photoreception: Opsin and Retinal Gene Expression in the Sea Urchin *Paracentrotus lividus*. *Cells* **11**, 2636 (2022).
35. Gonzalez, P., Uhlinger, K. R., & Lowe, C. J. The adult body plan of indirect developing hemichordates develops by adding a Hox-patterned trunk to an anterior larval territory. *Curr. Biol.* **27**, 87-95 (2017).
36. Wurst, W., & Bally-Cuif, L. Neural plate patterning: upstream and downstream of the isthmic organizer. *Nat. Rev. Neuro.* **2**, 99-108 (2001).
37. Darras, S. *et al*. Anteroposterior axis patterning by early canonical Wnt signaling during hemichordate development. *PLoS Biol.* **16**, e2003698 (2018).
38. Liu, P., Wakamiya, M., Shea, M. J., Albrecht, U., Behringer, R. R., & Bradley, A. Requirement for Wnt3 in vertebrate axis formation. *Nat. genet.* **22**, 361-365 (1999).
39. Krumlauf, R., Marshall, H., Studer, M., Nonchev, S., Sham, M. H., & Lumsden, A. Hox homeobox genes and regionalisation of the nervous system. *J. Neurobiol.* **24**, 1328-1340 (1993).
40. Martín-Zamora, F.M., *et al.* Annelid functional genomics reveal the origins of bilaterian life cycles. *Nature* **615**, 105-110 (2023).
41. Holley, S. A., Jackson, P. D., Sasai, Y., Lu, B., Robertis, E. M. D., Hoffmann, F. M., & Ferguson, E. L. A conserved system for dorsal-ventral patterning in insects and vertebrates involving *sog* and *chordin*. *Nature*. **376**, 249-253 (1995).
42. De Robertis, E. M., & Sasai, Y. A common plan for dorsoventral patterning in Bilateria. *Nature* **380**, 37-40 (1996).
43. Lee, K. J., & Jessell, T. M. The specification of dorsal cell fates in the vertebrate central nervous system. *Annu. Rev. Neurosci.* **22**, 261-294 (1999).
44. Yamada, M., Revelli, J. P., Eichele, G., Barron, M., & Schwartz, R. J. Expression of chick Tbx-2, Tbx-3, and Tbx-5 genes during early heart development: evidence for BMP2 induction of Tbx2. *Dev. Biol.* **228**, 95-105 (2000).
45. Timmer, J. R., Wang, C., & Niswander, L. BMP signaling patterns the dorsal and intermediate neural tube via regulation of homeobox and helix-loop-helix transcription factors. *Development* **129**, 2459–2472 (2002).
46. Barton-Owen, T. B., Ferrier, D. E., & Somorjai, I. M. *Pax3/7* duplicated and diverged independently in amphioxus, the basal chordate lineage. *Sci. Rep.* **8**, 9414 (2018).
47. Koop, D., Cisternas, P., Morris, V. B., Strbenac, D., Yang, J. Y. H., Wray, G. A., & Byrne, M. Nodal and BMP expression during the transition to pentamery in the sea urchin *Heliocidaris*

erythrogramma: insights into patterning the enigmatic echinoderm body plan. *BMC Dev. Biol.* **17**, 1-13 (2017).

48. Lowe, C. J., *et al*. Dorsoventral patterning in hemichordates: insights into early chordate evolution. *PLoS biol.* **4**, e291 (2006).
49. Panganiban, G., Irvine, S. M., Lowe, C., Roehl, H., Corley, L. S. et al. The origin and evolution of animal appendages. *PNAS*, **94**, 5162-5166.
50. Hotchkiss, F. H. A "rays-as-appendages" model for the origin of pentamerism in echinoderms. *Paleobiol*. **24**, 200-214 (1998).
51. Tarazona, O. A., Lopez, D. H., Slota, L. A., & Cohn, M. J. Evolution of limb development in cephalopod mollusks. *Elife*. **8**, e43828 (2019).
52. Lacalli, T. Echinoderm conundrums: Hox genes, heterochrony, and an excess of mouths. *EvoDevo* **5**, 1-4 (2014).
53. Yankura, K. A., Martik, M. L., Jennings, C. K., & Hinman, V. F. Uncoupling of complex regulatory patterning during evolution of larval development in echinoderms. *BMC Biol.*, **8**, 1-10 (2010).
54. Gąsiorowski, L., & Hejnol, A. Hox gene expression during development of the phoronid *Phoronopsis harmeri*. *EvoDevo*. **11**, 1-17 (2020).
55. True, J. R., & Carroll, S. B. Gene co-option in physiological and morphological evolution. *Annu. Rev. Cell Dev. Biol*. **18**, 53-80 (2002).
56. Zákány, J., & Duboule, D. Hox genes in digit development and evolution. *Cell Tissue Res.* **296**, 19-25 (1999).
57. Smith, A. B., & Zamora, S. Cambrian spiral-plated echinoderms from Gondwana reveal the earliest pentaradial body plan. *Proc. R. Soc. B: Biol. Sci.* **280**, 20131197 (2013).
58. Omori, A., Shibata, T. F., & Akasaka, K. Gene expression analysis of three homeobox genes throughout early and late development of a feather star *Anneissia japonica*. *Dev. Genes Evol.* **230**, 305-314 (2020).
59. Zamora, S., & Rahman, I. A. Deciphering the early evolution of echinoderms with Cambrian fossils. *Paleontology* **57**, 1105-1119 (2014).

Figure legends

Figure 1: Deployment of the antero-posterior patterning system in deuterostomes

a, Expression map of the conserved transcription factors and signaling ligands involved in ectoderm patterning along the AP axis, as observed in the hemichordate *Saccoglossus kowalveskii*. **b**, Previous work in chordates and hemichordates has demonstrated extensive regulatory conservation in ectodermal AP patterning, establishing the ancestral regulatory characteristics of early deuterostomes. How this system is deployed in echinoderms remains unclear. **c**, Four hypotheses have been proposed for the deployment of the AP patterning system in echinoderm adult body plan: bifurcation, circularization, duplication and stacking.

Figure 2: RNA tomography reveals the medio-lateral dimension of the arms as the main driver of antero-posterior patterning system deployment in *Patiria miniata*

a, Reconstructions of a young juvenile *P. miniata* scanned by micro-CT and segmented to highlight the endoskeleton (grey), the digestive tract (yellow), the main body muscles (red), the water vascular system (purple) and the central nervous system (blue). The ambulacral areas correspond to the grooves harboring the podia and are separated by interradial areas. Scale bar = 1mm. **b**, Experimental design of the RNA tomography with the cutting plans along the proximo-distal (P-D), oral-aboral (O-A) and medio-lateral (M-L) dimensions. **c**, Heatmap of gene expression z-scores along the P-D, O-A and M-L dimensions of the RNA tomography. **d**, Expression profiles of AP patterning related genes along the P-D, O-A and M-L dimensions of the RNA tomography. For the M-L dimension, the dotted line indicates the midline. Genes are ranked from the most anterior to the most posterior based on their expression patterns in *Saccoglossus kowalevskii*. **e**, Spearman correlations between the ranking of the AP patterning related genes and their position along the three dimensions of the RNA tomography. Dots indicate the raw correlation values. Boxplots indicate the distribution of correlation values when determining the gene position along each dimension probabilistically, and simultaneously shuffling the ranking of the AP patterning related genes for each group ($n = 10^6$ independent samples). The distribution of correlations for the M-L dimension is significantly higher than for the P-D and O-A dimensions (Two-sided Wilcoxon-rank test; $p < 10^{-4}$). Centre lines: median; box: interquartile range (IQR); whiskers: highest and lowest values at $\pm 1.5 \times$ IQR. **f**, Relative contribution of each group of AP patterning related genes to the Spearman correlation between the ranking of the AP patterning related genes and their position along the three dimensions of the RNA tomography.

Figure 3: Gene expression data reveals the deployment of the antero-posterior patterning system in *Patiria miniata* ambulacral ectoderm

a, Metamorphosis in *P. miniata*. The anterior part of the brachiolaria larva (cyan asterisk) is resorbed into the rudiment. **b**, HCRs showing *pax6* (red) and *otx* (cyan) starting to be expressed during metamorphosis in the developing adult pentaradial body plan. Specimens are counterstained with DAPI (blue). **c**, Main anatomical features of post-metamorphic juveniles, imaged from the oral side: the nervous system (cyan) stained with antibodies against acetylated-tubulin highlighting the nerve tracts and the neuronal marker *elav* highlighting the cell bodies, the hydrocoel stained with the marker *patched*, the digestive tract stained with the marker *lox* and the endoskeleton stained using calcein. RNC: radial nerve cord; CNR: circumoral nerve ring; RaC: radial canal; RiC: ring canal; St: stomach **d**, Schematics showing the oral-aboral position of the HCR z-projections shown in **e-κ** (top) and the main anatomical regions visible on the post-metamorphic juveniles oral side (bottom). The white square on the bottom panel indicates the position of the close-ups in **l,t,w,x,α,β**. **e-κ**, HCRs of *P. miniata* juveniles imaged from the oral side (**e-η**) or the aboral side (**θ-κ**). In **e-k,m-s,u,v,y,z,γ-κ,** specimens are counterstained with DAPI (blue). **l,t,w,x,α,β,** magnification of a single ambulacrum. **e-l**, Genes primarily expressed in the medial ambulacral ectoderm. Colocalization with *elav* indicates expression in the CNR and the RNCs. **m-t**, Genes primarily expressed in the podia epidermis. **u-β**, Genes primarily expressed in the ambulacral boundary. In **α,β,** orange dotted lines outline the ambulacral ectoderm. **γ-ζ**, Hox genes

primarily expressed in the coeloms. **η-κ**, Hox genes primarily expressed in the digestive tract. In **θ-κ,** red asterisks indicate the position of the developing intestinal tract. Scale bars = 100µm.

Figure 4: The ambulacral-anterior model of echinoderm body plan evolution

a, Expression map of the conserved transcription factors and signaling ligands involved in the ambulacral ectoderm patterning in *Patiria miniata*, organized from the midline of the ambulacrum (left) towards the interradius (right). **b**, Diagram of the ambulacral-anterior model in a generalized asteroid. Anterior patterning genes are expressed in the oral ambulacral ectoderm, shown through a cut-away of the forward part of the animal and a cross-section through the forward arm. Only genes expressed in the ectoderm are shown. **c,** Ambulacral-anterior model applied to echinoderm classes with available gene expression data, echinoids (left) and crinoids (right). In echinoids, the ambulacral ectoderm is internalized and shown through a cut-away of the forward part of the test, while in crinoids the ambulacral ectoderm is embedded in the oral epidermis, similar to asteroids.

Methods

Animal husbandry and tissue preparation

All animal collection and handling was done in compliance with US ethical regulations. Adult and young (~1-2cm wide) *Patiria miniata* specimens were collected off the coast of Monterey bay, California, US, and kept in circulating sea water tanks. Young specimens were used for X-ray micro-computed tomography (micro-CT), extract genomic DNA and RNA tomography (see below). For RNA tomography datasets and genomic DNA (see below), two young specimens of the same class of size than those used for micro-CT (referred to as specimens #1 and #2) were used. They were anesthetized in filtered sea water and 7.5% MgCl (1:1), and then four arms were dissected out. One of the arm was proceeded for DNA extraction, and the three others were included in HistoPrep embedding medium (ThermoFischer). Finally, to generate fixed material for HCRs and immunochemistry (see below), several batches of gravid adults were spawned by injecting 1ml of 1µM 1-methyladenine (Acros Organics) in each of the gonads. Sperm and mature oocytes were released by the animals about 45' and 90' after the injection, respectively. Following *in vitro* fertilization, embryos were cultured at 14°C in UV-sterilized filtered seawater, first at a density of about 100 embryos per mL and within 3L glass jars oxygenated by a motorized paddle. At 48 hours post fertilization, the culture concentration was adjusted to about 1 larva per mL, and from that point about 95% of the seawater was renewed every 2 or 3 days. Following water renewal, the larvae were fed *ad libidum* with freshly grown *Rhodomonas lens* microalgae. Brachiolaria larvae started to settle on the glass jars and to undergo metamorphosis between 1 and 2 months post fertilization. After metamorphosis, juveniles were collected from the glass jars by being first relaxed in a 1:1 mix of 7.5% $MgCl_2$ and filtered seawater and then being gently detached using a paintbrush.

X-ray micro-computed tomography

For X-ray micro-CT analyses, *P. miniata* young juveniles of the same size than those used for RNA tomography were relaxed in a 1:1 mix of 7.5% $MgCl_2$ and filtered seawater for 10', and then fixed in a modified PHEM buffer[60] (90mM PIPES, 37mM HEPES, 14mM EGTA, 30mM $MgCl_2$, 9% fructose) overnight at 4°C. The samples were then washed in modified PHEM buffer, before being counterstained in 2% osmium tetroxide in deionized water for two hours. Following staining, the samples were washed extensively in deionized water, gradually dehydrated in ethanol and stored in ethanol at 4°C. Prior to imaging, samples were dried and then pinned on their aboral side to an imaging support. Scanning was carried out using a Zeiss Xradia 520 Versa 3D X-ray microscope. Specimens were scanned at a resolution of 12.138µm per voxel. In order to identify different tissues in the scans, regions of interest were segmented using Dragonfly v.2022.2. For segmentation, the deep learning tool was used to train a 3D U-net model, which has been shown to be ideal for rapid and accurate automatic biomedical image segmentation[61]. The U-net model had nine classes, corresponding to different tissue types, and was trained for 75 epochs (15.5 hours) using a training set of fifteen manually segmented slices from the dataset. During model training, a data augmentation factor of 2 was used, including horizontally and vertically slipping the data, rotation, shearing, and zoom. Following model training, this U-net was used to automatically segment and identify our nine different tissue classes. Following the initial deep learning-based segmentation, the nine classes were reduced to the five regions of interest shown in the 3D model (endoskeleton, digestive tract, musculature, water vascular system, and central nervous system) *via* the merging of classes relating to similar tissue types (for instance, combining classes pertaining to different types of endoskeletal tissue). At this point, further segmentation was carried out manually in Dragonfly to clean up regions of interest and to produce 3D models and mesh files for visualization. After segmentation, the consistency between the size of the anatomical features reconstructed from the micro-CT scans and the extent of tissue marker expression profiles from the RNA tomography was checked manually. The samples used for micro-CT were registered at the Natural History Museum (London, UK) under the registration number NHMUK 2023.263. The segmented scans and reconstructed mesh files were deposited on Morphosource under the project number 000529415.

Genomic DNA isolation

Genomic DNA (gDNA) for genome sequencing was isolated from a dissected arm of the young *P. miniata* specimen #1. Using an extended handle conical tip pestle (Bel-Art Proculture), the arm was homogenized in the presence of the extraction buffer and of proteinase K. Genomic DNA was then isolated using the DNeasy Blood and Tissue Kit (Qiagen) following the manufacturer's instructions.

Genome sequencing

Ultra-Low Input HiFi library preparation

Using gDNA from the arm of specimen #1, we generated a HiFi genome of *P. miniata*. The general workflow is described in Supplementary Fig.2e. As the gDNA isolated from the arm was predominantly shorter than the 10-15 kb which is recommended size for HiFi genomic library creation, a size selection was performed prior to doing an Ultra-Low Input (ULI) amplification and library preparation to remove fragments <7kb. The size selection was done on a SAGE BluePippin system using the 0.75% Agarose Dye-free Gel Cassette and the S1 Marker (SAGE). Approximately 100ng of DNA was recovered post size selection and used as input for the ULI PCR-based HiFi library protocol. The sample was amplified using the SMRTbell gDNA Amplification Kit (PacBio) and a HiFi SMRTbell library was constructed using the SMRTbell Express Template Prep Kit 2.0 (PacBio) following manufacturer's recommended protocol. After library construction, a final size selection was performed on the SAGE BluePippin as previously described using a size cut-off of 7kb. Library size was characterized on an Agilent 2100 BioAnalyzer using the DNA 12000 kit (Agilent). The additional size selection ensured having a final library with a fragment size range greater than 7kb.

HiFi reads sequencing

Sequencing reactions were performed on the PacBio Sequel II System with the Sequel Sequencing Kit 2.0 (PacBio). The kit uses a circular consensus sequencing (CCS) mode which provides >99.5% single molecule read accuracy[62]. The samples were pre-extended without exposure to illumination for 2 hours to enable the polymerase enzymes to transition into the highly progressive strand-displacing state and sequencing data was collected for 30 hours to ensure maximal yield of high-quality CCS reads. CCS reads were generated from the data using the SMRT Link Version 9.0 (PacBio). For the genomic HiFi sequencing, the library was bound to the sequencing enzyme using the Sequel II Binding Kit 2.2 and the Internal Control Kit 1.0 (PacBio). The HiFi reads generated 15,614,751 HiFi reads with a mean read length of 9,039 bp ± 1,671bp (Supplementary Fig. 3e).

Genome assembly

Prior to *de novo* genome assembly, the reads were trimmed on the ends to remove any PCR primer sequences from the ultra-low amplification process using lima v.2.2 (PacBio). The forward sequence of the amplification adapter used was AAGCAGTGGTATCAACGCAGAGTACT. Once the HiFi reads were trimmed, a filtering step was performed to remove duplicate reads from the PCR step using SMRT link v.9.0. After removing duplicate reads, the HiFi reads (~100X genomic coverage) were used to generate a draft diploid assembly using Hifiasm v.0.15[63]. This resulted in two highly contiguous haplotype primary assemblies of 680 Mb and 674 Mb respectively (Supplementary Table 5). Assembly completeness was assessed with the Benchmarking Single Copy Ortholog[64] (BUSCO v.3.0) gene set for Metazoa at 94.8% for each of the individual haplotype primary assemblies and 96.2% overall for the diploid assembly as a whole (Supplementary Fig.3d; Supplementary Table 4). The two haplotypes were deposited at DDBJ/ENA/GenBank under the accession number JAPJSQ000000000 and JAPJSR000000000.

RNA tomography section preparation and RNA extraction

The three arms embedded in HistoPrep medium were cryosectioned using a Leica CM3050-S microtome along the appropriate dimensions: proximo-distal (P-D), oral-aboral (O-A) or medio-lateral (M-L) (Supplementary Fig.2a-c). The blocks used for the P-D and O-A dimensions came from the specimen #1, while the block used for the L-R dimension came from the specimen #2. Slice thickness was set to 25µm for the P-D and O-A dimensions and to 30µm for the M-L dimension, resulting in total in 430, 160 and 160 slices for the three respective dimensions. While sectioning the blocks, every 20 (P-D, O-A) or 10 (M-L) contiguous slices were pooled together into 1.5mL tubes. These resulted in a total of 22 tubes for the P-D dimension, 8 tubes for the O-A dimension and 16 tubes for the L-R dimension (Supplementary Fig.2d). Each tube was then processed for RNA extraction using a modified Trizol/RNeasy RNA extraction protocol[65]. In each tube the slices were homogenized in 1mL of Trizol using an extended handle conical tip pestle (BelArt Proculture). After vigorously mixing the Trizol homogenate with chloroform, each tube was centrifuged at 10,000xg RCF for 18' at 4° C. The aqueous phase containing the RNA was carefully removed and the RNA was further purified using the RNeasy Plus Micro Kit (Qiagen) following the manufacturer's instructions.

RNA tomography

Barcoded cDNA IsoSeq SMRTbell library preparation

Using RNA isolated from the three sets of cryosections, we generated a RNA tomography[28,66] dataset for *P. miniata* juveniles. The general workflow is described in Supplementary Fig.2e. Barcoded PacBio IsoSeq SMRTbell libraries were constructed using the SMRTbell Express Template Prep Kit 2.0 (PacBio) following the manufacturer's instructions. We used a set of 22 barcoded sequences (Supplementary Table 1) which were combined with each RNA extracts (Supplementary Table 2). Typically, 12-14 PCR amplification cycles were used to generate enough barcoded double-stranded cDNA for the library preparation and subsequent sequencing runs (Supplementary Table 2).

Library sequencing

For the IsoSeq transcript libraries, library was bound to the sequencing enzyme using the Sequel II Binding Kit 2.1 and Internal Control Kit 1.0 (PacBio) and the sequencing reactions were performed on the PacBio Sequel II System. The three dimensions were sequenced independently, since there were shared barcodes between the different libraries. We obtained a total of 71,582,642 reads (Supplementary Table 3) with a mean read length of 3,843bp, 3,152bp and 2,450bp for the P-D, O-A and L-R dimensions, respectively (Supplementary Fig.3a). In addition, HiFi read length distributions were consistent across each barcode within the respective RNA tomography dimension (Supplementary Fig.3b). Sequence read archives were deposited at DDBJ/ENA/GenBank under the bioproject PRJNA873766 and individual accession numbers for each barcode are provided in Supplementary Table 3. Recent advancements in full length transcript concatenation protocols[67], as well as higher multiplexed SMRT sequencing flow cells have increased throughput with a concomitant decrease in sequencing cost over a single 24 hour run. Genomic, epigenetic and transcript data sets can now all originate from the same individual greatly improving the mappability and subsequent analysis of transcripts in highly polymorphic non-model organisms where gene sequences can differ by >5% in coding regions and as much as 40% in UTR sequence which complicate short read transcript alignment and reliable quantitation.

IsoSeq reads demultiplexing and refining

For each HiFi read file generated, the data was demultiplexed into barcode specific read files using lima v.2.2 (PacBio) and the barcodes listed in Supplementary Table 1. Once the data were demultiplexed each read file was refined to include only full length non-chimeric reads using isoseq3 v.3.4.0[68]. Chimeras were identified by inclusion of 5' or 3' RT-PCR primer sequences internal to the initial 'full length' HiFi read. The primer sequences used were NEB_5P (GCAATGAAGTCGCAGGGTTGGG),

Clontech_5P (AAGCAGTGGTATCAACGCAGAGTACATGGGG), and NEB_Clontech_3P (GTACTCTGCGTTGATACCACTGCTT). Transcript clusters were identified using Cupcake v.25.2.0[69] which leverages a genomic reference alignment-based strategy to identify redundant isoforms/transcripts for gene loci. We leveraged the diploid assembly to minimize dropouts that might be caused by haplotype specific null alleles and/or poor mapping between haplotypes for the same locus. Comparative alignment of the two haplotype derived transcriptomes facilitated further collapse of the gene set to one representative per loci.

Transcriptome generation and curation

Using each haplotype primary assembly, the complete set of full length non-chimeric transcript reads (FLNC) were clustered and collapsed to reduce gene redundancy while maintaining the highest possible level of gene completeness. The complete set of FLNC reads across all three combined RNA tomography datasets were clustered from a list of input bam files based on each of the haplotype specific primary assemblies. Minimap2 v.2.21[70] was used to align the FLNC reads to each primary assembly and Sqanti2 v.7.4[71] was used to cluster and filter redundancies. Once minimal transcript sets were obtained for each haplotype, a comparative alignment between the sets was performed using Minimap2 v.2.21 aligner to find unique transcripts between the two. From the ouput paf files, transcripts unique to haplotype 2 which were not present in the haplotpye 1 were identified, filtered out from the haplotype 2 set, and added to the Haplotype 1 set to obtain a more complete single copy transcript set.

Manually curated developmental genes of interest were identified (see below). All sequence in our "single copy" transcript set were aligned using TBLASTX to the manually curated set to (1) remove any duplication of these key transcripts in our reference transcriptome (e.g. the high polymorphism rate resulted in both copies of some of the manually curated genes being present) and (2) remove partial duplications (non-full length transcripts matching the manually curated set). The result of this curation step was to ensure that for every gene of interest, we had only one sequence in our reference transcriptome to maintain accurate downstream quantification. Given the occasional duplication of transcripts in our reference transcriptome (eliminated for our genes of interest), it is assumed that the un-curated transcripts have some level of duplication.

Once we derived a near complete curated transcriptome for *P. miniata*, the barcode specific demultiplexed RNA tomography datasets were aligned to the transcriptome reference using Minimap2 v.2.21. The final refined *P. miniata* transcriptome comprised 25,794 transcripts and represented a nearly complete (91.5%) set of metazoan BUSCO genes (Supplementary Fig.3d; Supplementary Table 4). Transcript expression counts for each of the 25,794 gene model in our reference transcriptome were tallied using a simple Perl v.5.30.1 script that only counted primary alignments (no supplementary alignments) with a quality value of 15 or greater. Each section was tallied independently and the data merged. The alignment counts for each section were normalized to the total reads for each barcode in order to allow spatial comparisons to be made across each dimension of the RNA tomography dataset. This was done to account for variable recovery of total RNA in each barcoded section. (Supplementary Fig.3c).

<u>Orthologues identification</u>

P. miniata orthologues of developmental genes of interest, which included 36 AP patterning related genes, 6 DV specification and patterning related genes, 3 limb proximo-distal patterning related genes, the pan-neuronal marker *elav*, the gut marker *lox* and the hydrocoel marker *patched* were identified from the FLNC reads by reciprocal best blast hit and validated by phylogenetic trees (Supplementary Fig.4). Nucleotide sequences for these transcripts were deposited at DDBJ/ENA/GenBank and accession numbers are provided in Supplementary Table 6. Trees were calculated with both the Maximum likelihood and Bayesian inference methods. Maximum likelihood trees were calculated in MEGA v.7.0.26[72] with the robustness of each node being estimated by bootstrap analyses (in 1000 pseudoreplicates). Bayesian inference trees were calculated using MrBayes v.3.1.2[73] in 1,000,000 generations with sampling of trees every 100 generations and a burn-in period of 25%. The branching

pattern of the ML tree was retained in the final tree figure, displaying, at each node, the bootstrap support of the ML analysis as well as the posterior probability support of the BI analysis.

RNA tomography analyses

RNA tomography analyses were performed in R v.4.1.2 using custom-written code. For downstream analyses, the 22 sections of the P-D were merged pairwise by simple addition of the read counts mapping for each transcripts, bringing the final number of sections in the P-D dimensions to 11 (Supplementary Fig.2d). In addition, section 14 of the M-L dataset was removed because it yielded a total read count 77% lower than the average total read count per section for the M-L dimension, which could have biased the quantification analyses. To maintain the symmetry in the M-L dimension, section 3 was also removed, bringing the final number of sections in the M-L dimension to 14 (Supplementary Fig.2d).

Individual read counts from each section of the three RNA tomography dimensions were normalized against the total read count of the section in order to account for sequencing depth differences between the three dimensions and for geometrical disparities between the different sections of a single dimension. Because we were interested in the profile of highly expressed and variable genes, whereas genes with a uniform expression across the sections were poorly informative, a cutoff was applied to discard genes which consistently had the 20% lowest average expression level or 20% lowest variability in all of the three dimensions, resulting in a final set of 21,847 gene models (Supplementary Fig.3f). Of the 36 AP patterning related genes investigated in this study, four of them fell below the cutoff and were excluded from the computational analyses because of their low expression levels: *rx*, *dlx*, *hox11/13a*, and *hox11/13c* (Supplementary Fig.3f). For further analyses, the expression levels of each gene along each of the three dimension sections was transformed into z-score.

For the clustering analysis, the dimensionality of the dataset was first reduced using a principal component analysis (PCA) performed simultaneously on the three dimensions of the RNA tomography. Kaiser-Guttman's criterion[74] was used to select the significant PCs of the PCA. Then, the coordinates of the transcripts along the retained PCA axes were used to compute the Euclidean distance matrix and hierarchical agglomerative clustering using Ward's aggregation to produce an expression profile dendrogram[75]. Following the methodology established in previous RNA tomography studies[28], we estimated a maximal number of 12 clusters based on discernible anatomical features in the Spearman correlation matrices of the sections (Extended Data Fig. 1f). However, the relevant number of clusters was likely lower than 12 due to the lack of independence of gene expression between the three dimensions. We thus used a silhouette index[76] to evaluate the consistency of clusters when choosing between 2 and 12 clusters. The silhouette index indicated that 7 was the most appropriate number of clusters, and this number also minimized redundancy between the different dimensions.

For the hypothesis testing, we determined the ranking of the 36 investigated AP patterning related genes based on their expression profiles in the hemichordate *S. kowaleskii*, which is the closest bilateral echinoderm-relative with an extensive dataset of AP patterning gene expression profiles[4,5,37,48,77-80]. Gene expression patterns in other hemichordate studies are largely consistent with those observed in *S. kowalevskii*[35,81]. The 36 genes were divided into seven groups based on their expression domains (anterior proboscis (A), proboscis (B), anterior collar (C), posterior proboscis and collar (D), collar-trunk boundary (E), trunk (F), posterior tip of the trunk (G)) (Supplementary Fig.6). Within each group, genes were ranked based on their expression pattern, and, when required, tied based on the available gene expression patterns in other closely related species. We were confident that the assignment of each gene to the groups A to G based on their expression profile in *S. kowalevskii* was robust to interpretation biases. On the other hand, given that the genes expressed in these groups are more or less coincident in parts of the AP axis of *S. kowalevskii,* we recognized that the internal gene ranking within each group was more subject to possible interpretation biases.

To test the Spearman correlation between the AP patterning related gene ranking and the gene expression profiles along the three dimensions of the RNA tomography, the symmetrical sections of the M-L were averaged pairwise (1 and 14; 2 and 13; and so on). We then used the highest z-score as a

readout for the position of each gene in each dimension, and correlated it to the ranking of the AP genes as described above. The significance of this raw correlation was assessed by a two-sided Spearman correlation test. In addition, each of the seven group of genes was independently removed to assess its contribution to the correlation. However, this approach is subjected to two potential sources of errors, resulting from (1) choosing the single highest z-score value for the position of genes with multimodal expression profiles, and (2) and as mentioned above from biases in determining the ranking of the AP genes within each of the seven gene groups, as mentioned above. To account for these biases, we also ran 10^6 independent correlations, with each correlation (1) probabilistically determining the position of each gene by using the z-score as a law of probability, and (2) randomly shuffling the ranking of the genes within the seven gene groups. The distribution of the 10^6 correlation values was then compared across the three dimensions of the RNA tomography using a two-sided Wilcoxon rank test.

In situ hybridization

Short *in situ* hybridization antisens DNA probes were designed based on the split-probe design of HCR v.3.0[82] using HCR 3.0 Probe Maker[83] with adjacent B1, B2 or B3 amplification sequences depending on the genes (Supplementary Table 7). Between 14 and 33 probe pairs were designed for each gene including the CDS, and for some of them adjacent 5' and 3' UTRs. The probe pairs were then ordered as oligo pools (Integrated DNA Technology) and suspended in nuclease-free water at a concentration of 0.5µM.

For *In situ* hybridization, *P. miniata* brachiolaria larvae, metamorphosing larvae and juveniles were incubated in fixation buffer (1X phosphate buffered saline (PBS), 0.1M MOPS, 0.5M NaCl, 2mM EGTA, 1mM $MgCl_2$) containing 3.7% formaldehyde overnight at 4°C. Fixed samples were then dehydrated in methanol and stored at -20°C for at least 24 hours and up to several months. The samples were progressively rehydrated in PBS containing 0.1% Tween-20 (PBST). They were permeabilized in detergent solution (1.0% SDS, 0.5% Tween-20, 150mM NaCl, 1mM EDTA (pH 8), 50mM Tris-HCl at pH 7.5) 30' for larvae and 2 hours for juveniles. For juveniles, this was step was followed by an extra permeabilization step in 4µg/mL proteinase K (Sigma-Aldrich) for 10' at 37°, and a postfixation in 3.7% formaldehyde for 25'. The samples were then extensively washed in PBST, and then in 5X saline sodium citrate buffer containing 0.1% Tween-20 (SSCT), before being pre-hybridized in hybridization buffer (Molecular Instruments) for 1h at 37°C. The probes were then added to the hybridization buffer at a final concentration of 0.05µM and the samples were let to hybridize at 37°C overnight under gentle agitation. Following hybridization, the samples were washed 4 times 30' in probe wash buffer (Molecular instruments) at 37°C and then in 5X SSCT at room temperature. They were then pre-amplified in amplification buffer (Molecular Instruments) for 30'. Meanwhile, H1 and H2 components of the HCR hairpins B1, B2 or B3 coupled either to Alexa546 or Alexa647 fluorophores (Molecular Instruments) were incubated separately at 95°C for 90", cooled down to room temperature in the dark and then pooled together before being added to the amplification buffer at a final concentration of 60nM. The amplification was then performed overnight at room temperature. The samples were subsequently washed 4 times 30' in 5X SSCT and incubated in PBST containing 1:1000 DAPI (Invitrogen) for three hours. Finally, the samples were cleared in a series of 20%, 40%, 60%, and 80% fructose diluted in NaCl-PBS. Each fructose bath was carried out for at least 1 hour. Clarified samples were mounted in 80% fructose diluted in PBS for imaging, which was done using a Zeiss LSM700 confocal microscope. For each sample, series of optical sections were taken with a z-step interval of 2-3µm Multichannel acquisitions were obtained by sequential imaging. Confocal optical sections spanning regions of interest along the oral-aboral axis were compiled into maximum intensity z-projections using ImageJ v.1.52g[84] and assemble into figure using Adobe Illustrator v.15.0.0.

The specificity of the antisens DNA probes and amplification hairpins was validated by running the protocol without hairpins and probes or with hairpins alone, and comparing antisens and sense probe sets for *nkx2.1* (Supplementary Fig.7). The consistency of the expression patterns obtained through this method was further validated by comparisons of *elav*, *nkx2.1*, *dmbx* and *otx* with colorimetric whole-mount *in situ* hybridization using single antisens RNA probes as described previously[85] (Supplementary Fig.7). To ensure reproducibility of the *in situ* hybridization expression patterns, each gene was surveyed

811 in at least two independent experiments, and for each experiment at least 10 samples were analyzed and
812 gave consistent results.

813 Immunohistochemistry

814 Immunofluorescence stainings were performed as described previously[86] using an anti-acetylated
815 tubulin antibody produced in mouse (Sigma aldrich, Reference #T7451-100UL, Lot #036M4856V)
816 diluted at 1:200. Secondary antibody used was a goat anti-mouse IgG (H+L) secondary antibody coupled
817 to Alexa Fluor 647 (Invitrogen, Reference #A21235, Lot 2270554) diluted at 1:500. For endoskeleton
818 stainings, larvae reaching the brachiolaria stage were incubated in seawater supplemented with 5mL per
819 1L of saturated calcein solution (Sigma-Aldrich), a fluorescent calcium analogue that is incorporated
820 into the endoskeleton[87], until the completion of the metamorphosis. The post-metamorphic juveniles
821 were then fixed, counter-stained with DAPI and cleared following the same procedure than for
822 immunofluorescence stainings. Imaging was done following the same procedure than for *in situ*
823 hybridizations.

Methods references

60. Montanaro, J., Gruber, D., & Leisch, N. Improved ultrastructure of marine invertebrates using non-toxic buffers. *PeerJ 4*, e1860 (2016).
61. Ronneberger, O., Fischer, P., Brox, T. U-Net: Convolutional Networks for Biomedical Image Segmentation. In: Navab, N., Hornegger, J., Wells, W., Frangi, A. (eds) Medical Image Computing and Computer-Assisted Intervention – MICCAI 2015. Lecture Notes in Computer Science, vol 9351. Springer, Cham (2015).
62. Wenger, A.M., Peluso, P., Rowell, W.J. et al. Accurate circular consensus long-read sequencing improves variant detection and assembly of a human genome. *Nat. Biotechnol.* **37**, 1155–1162 (2019).
63. Cheng, H., Concepcion, G. T., Feng, X., Zhang, H., & Li, H. Haplotype-resolved de novo assembly using phased assembly graphs with hifiasm. *Nat. methods* **18**, 170-175 (2021).
64. Simão, F. A., Waterhouse, R. M., Ioannidis, P., Kriventseva, E. V., & Zdobnov, E. M. BUSCO: assessing genome assembly and annotation completeness with single-copy orthologs. *Bioinform.* **31**, 3210-3212 (2015).
65. Bellantuono, A.J., Granados-Cifuentes, C., Miller, D.J., Hoegh-Guldberg, O., & Rodriguez-Lanetty, M. Coral thermal tolerance: tuning gene expression to resist thermal stress. *PloS one* **7**, e50685 (2012).
66. Kruse, F., Junker, J. P., Van Oudenaarden, A., & Bakkers, JTomo-seq: A method to obtain genome-wide expression data with spatial resolution. *Methods Cell. Biol.* **135**, 299-307 (2016).
67. Al'Khafaji, A. M., *et al*. High-throughput RNA isoform sequencing using programmable cDNA concatenation. *bioRxiv* (2021).
68. Mattick, J. IsoSeq v3. Available online: https://github.com/PacificBiosciences/IsoSeq
69. Tseng, E. cDNA cupcake. Available online: https://github.com/Magdoll/cDNA_Cupcake/wiki.
70. Li, H. Minimap2: pairwise alignment for nucleotide sequences. *Bioinform.* **34**, 3094–3100 (2018).
71. Tardaguila, M., *et al*. SQANTI: extensive characterization of long-read transcript sequences for quality control in full-length transcriptome identification and quantification. *Genome Res.* **28**, 396–411 (2018).
72. Kumar, S., Stecher, G. & Tamura, K. MEGA7: Molecular Evolutionary Genetics Analysis version 7.0 for bigger datasets. *Mol. Biol. Evol.* **33**, 1870-1874 (2016).
73. Huelsenbeck, J. P., & Ronquist, F. MRBAYES: Bayesian inference of phylogenetic trees. *Bioinform.* **17**, 754-755 (2001).
74. Guttman, L. Some necessary conditions for common-factor analysis. *Psychometrika* **19**, 149-161 (1954).
75. Murtagh, F., & Legendre, P. Ward's hierarchical agglomerative clustering method: which algorithms implement Ward's criterion? *J. Classif.* **31**, 274-295 (2014).
76. Rousseeuw, P. J. Silhouettes: a graphical aid to the interpretation and validation of cluster analysis. *J. Comput. Appl. Math.* **20**, 53-65 (1987).
77. Aronowicz, J., & Lowe, C. J. Hox gene expression in the hemichordate *Saccoglossus kowalevskii* and the evolution of deuterostome nervous systems. *Int. Comp. Biol.* **46**, 890-901 (2006).
78. Lemons, D., Fritzenwanker, J. H., Gerhart, J., Lowe, C. J., & McGinnis, W. Co-option of an anteroposterior head axis patterning system for proximodistal patterning of appendages in early bilaterian evolution. *Dev. Biol*. **344**, 358-362 (2010).
79. Satoh, N. et al. On a possible evolutionary link of the stomochord of hemichordates to pharyngeal organs of chordates. *Genesis* **52**, 925-934 (2014).
80. Fritzenwanker, J. H., Uhlinger, K. R., Gerhart, J., Silva, E., & Lowe, C. J. Untangling posterior growth and segmentation by analyzing mechanisms of axis elongation in hemichordates. *Proc. Natl. Acad. Sci.* **116**, 8403-8408 (2019).
81. Kaul-Strehlow, S., Urata, M., Praher, D., & Wanninger, A. Neuronal patterning of the tubular collar cord is highly conserved among enteropneusts but dissimilar to the chordate neural tube. *Sci. Rep.* **7**, 1-10 (2017).
82. Choi, H. M., Schwarzkopf, M., Fornace, M. E., Acharya, A., Artavanis, G., Stegmaier, J., Cunha, A. & Pierce, N. A. Third-generation in situ hybridization chain reaction: multiplexed, quantitative, sensitive, versatile, robust. *Development* **145**, dev165753 (2018).

83. Kuehn, E., Clausen, D. S., Null, R. W., Metzger, B. M., Willis, A. D., & Özpolat, B. D. (2022). Segment number threshold determines juvenile onset of germline cluster expansion in *Platynereis dumerilii*. *J. Exp. Zool. B: Mol. Dev. Evol* **338**, 225-240.
84. Schneider, C. A., Rasband, W. S., & Eliceiri, K. W. NIH Image to ImageJ: 25 years of image analysis. *Nat. methods* **9**, 671-675 (2012).
85. Lowe, C.J., Tagawa, K., Humphreys, T., Kirschner, M., & Gerhart, J. Hemichordate embryos: Procurement, culture, and basic methods. *Methods Cell. Biol.* **74**, 171–194 (2004).
86. Formery, L., Orange, F., Formery, A., Yaguchi, S., Lowe, C. J., Schubert, M., & Croce, J. C. Neural anatomy of echinoid early juveniles and comparison of nervous system organization in echinoderms. *J. Comp. Neurol*. **529**, 1135-1156 (2021).
87. Thompson, J. R., Paganos, P., Benvenuto, G., Arnone, M. I., & Oliveri, P. Post-metamorphic skeletal growth in the sea urchin *Paracentrotus lividus* and implications for body plan evolution. *EvoDevo* **12**, 1-14 (2021).

Acknowledgements

The authors would like to thank Fabio Benedetti and Robin Elahi for helping with RNA tomography analyses; Arturas Vailionis, Pranav Vyas and the Stanford Nano Shared Facility for helping with X-ray micro-computed tomography; Jennifer Grossman for the ambulacral-anterior model schematics; Antoine Formery for providing the 3D models of the RNA tomography sections; Auston Rutledge for helping with animal husbandry; and Veronica Hinman for providing clones for preliminary analyses. The authors also thank Gregory A. Wray, Thurston Lacalli, Rich Mooi, Jenifer C. Croce, and members of the Rokhsar and Lowe laboratories for discussions. This work was supported by a Leverhulme Trust Early Career Fellowship to J.R.T., a NASA grant to C.J.L. (NNX13AI68G), a NSF grant to C.J.L. (1656628) and Chan Zuckerberg BioHub funding to D.S.R. and C.J.L. For the purpose of open access, the author has applied a CC BY public copyright license to any Author Accepted Manuscript version arising from this submission.

Authors contribution

Experiments were designed by L.F., P.P., D.R.R. and C.J.L. Preliminary data were acquired by I.K., J.M. and K.R.U. Genome sequencing was done by P.P. and D.R.R. RNA tomography sectioning and sequencing was done by P.P., M.P., D.R.R. and C.J.L. RNA tomography analyses were performed by L.F. and D.S.R. Micro-computed tomography preparation was done by L.F. and segmentation of the scans was done by J.R.T. Immunofluorescence, HCRs and imaging were performed by L.F. Data were analyzed by L.F, D.S.R. and C.J.L. The manuscript was written by L.F., D.S.R., and C.J.L. with input from all authors.

Conflict of interests

P.P. and D.R.R. are employees and shareholders of Pacific Biosciences. Other authors declare no conflict of interests.

Supplementary information

Supplementary Information is available for this paper. Correspondence and requests for materials should be addressed to L.F. Reprints and permissions information is available at www.nature.com/reprints.

Data availability

Specimens used for Micro-CT analyses are registered at the Natural History Museum (London, UK) under the registration number NHMUK 2023.263. The segmented scans and reconstructed mesh files are available in Morphosource under the project number 000529415. Genome haplotypes are available at DDBJ/ENA/GenBank under the accession number JAPJSQ000000000 and JAPJSR000000000. Sequence read archives for RNA sequencing are available at DDBJ/ENA/GenBank under the bioproject PRJNA873766. RNA tomography dataset is available at Zenodo under DOI 10.5281/zenodo.8327479.

Code availability

Custom code used for RNA tomography analyses is available at Zenodo under DOI 10.5281/zenodo.8327479.

Extended Data

Extended Data Figure 1: *Patiria miniata* anatomy is reflected by RNA tomography

a, Phylogenetic position of *P. miniata* within deuterostomes, the grey box highlights the echinoderm phylum. **b**, Young adult *P. miniata*, viewed from the aboral side. **c,d,** Reconstructions of a young juvenile *P. miniata* scanned by micro-CT and segmented to highlight the main anatomical features of the animal, including the endoskeleton (grey), the digestive tract (yellow), the main body muscles (red), the water vascular system (WVS; purple) and the central nervous system (CNS; blue). **c,** Lateral views showing virtual sections of the micro-CT reconstruction along the proximo-distal (P-D), oral-aboral (O-A) and medio-lateral (M-L) dimensions used in the RNA tomography. Scale bar = 1mm. **d,** Details of the different anatomical features shown in aboral or lateral views. The different panels are shown at the same scale. TAM: transverse ambulacral muscle; LTAM: lateral transverse ambulacral muscle; Long. M: longitudinal muscle; RNC: radial nerve cord; CNR: circumoral nerve ring. **e,** Principal component analysis of the RNA tomography sections. For each dimension the sections are color-coded according to the geometry of the animal. **f,** Spearman correlations between the sections of the RNA tomography in each of the three dimensions. Epi: epidermis; Amb: ambulacrum. **g,** Expression profiles along the three dimensions of the RNA tomography for tissue marker genes known based on published literature to be expressed in the endoskeleton (grey), digestive tract (yellow), muscles (red), WVS (purple) and in the nervous system (blue) are consistent with the anatomy of the animal. Note that in the case of digestive tract markers, there is a left shift of expression in the L-R dimension that we assume resulted from displacement of the pyloric caeca during the dissection of the arm.

Extended Data Figure 2: Dorso-ventral and appendage patterning in *Patiria miniata*

a, Schematic representation of DV patterning in bilaterians. **b,** Expression profile of DV specification and patterning genes along the P-D, O-A and M-L dimensions of the RNA tomography. For the M-L dimension, the dotted line indicates the midline. **c-v,y-α,** HCRs of *P. miniata* brachiolaria (**c,h,m**), early metamorphosis (**d,i,n**), late metamorphosis (**e,j,o**) and post-metamorphic juveniles (**f,g,k,l,p-v, y-α**) imaged from the oral side. In **c-q,t,u,y-α,** specimens are counterstained with DAPI (blue). **g,l,q,r,s,v**, Magnification of a single ambulacrum. **c-v,** Expression patterns of genes involved in DV axis specification and patterning. **w,** Schematic representation of limb proximo-distal patterning in bilaterians. **x**, Expression profile of limb proximo-distal patterning genes along the P-D dimension of the RNA tomography. **y-α,** Expression patterns of genes involved in limb proximo-distal patterning. Scale bars = 100µm.

Figures

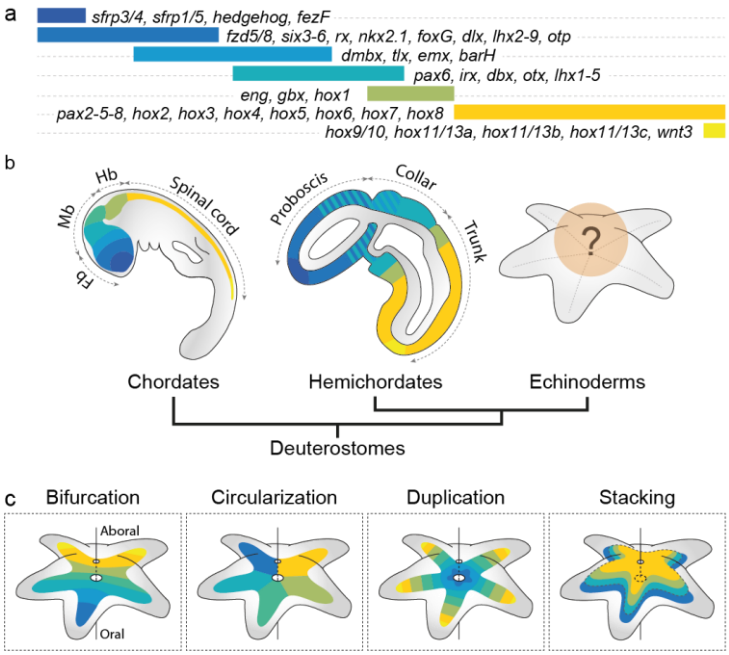

Figure 1: Deployment of the antero-posterior patterning system in deuterostomes

a, Expression map of the conserved transcription factors and signaling ligands involved in ectoderm patterning along the AP axis, as observed in the hemichordate *Saccoglossus kowalveskii*. **b**, Previous work in chordates and hemichordates has demonstrated extensive regulatory conservation in ectodermal AP patterning, establishing the ancestral regulatory characteristics of early deuterostomes. How this system is deployed in echinoderms remains unclear. **c**, Four hypotheses have been proposed for the deployment of the AP patterning system in echinoderm adult body plan: bifurcation, circularization, duplication and stacking.

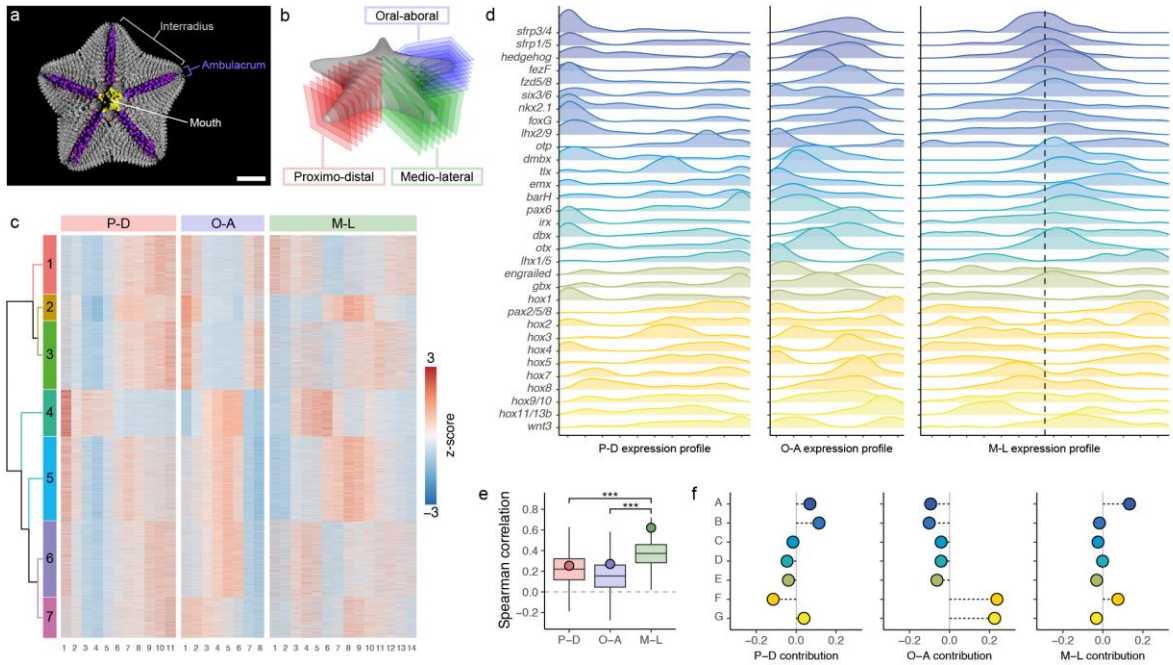

Figure 2: RNA tomography reveals the medio-lateral dimension of the arms as the main driver of antero-posterior patterning system deployment in *Patiria miniata*

a, Reconstructions of a young juvenile *P. miniata* scanned by micro-CT and segmented to highlight the main anatomical features of the animal, including the endoskeleton (grey), the digestive tract (yellow), the main body muscles (red), the water vascular system (purple) and the central nervous system (blue). The ambulacral areas correspond to the grooves harboring the podia and are separated by interradial areas. Scale bar = 1mm. **b**, Experimental design of the RNA tomography with the cutting plans along the proximo-distal (P-D), oral-aboral (O-A) and medio-lateral (M-L) dimensions. **c**, Heatmap of gene expression z-scores along the P-D, O-A and M-L dimensions of the RNA tomography showing seven main trends of spatial expression. **d**, Expression profiles of AP patterning related genes along the P-D, O-A and M-L dimensions of the RNA tomography. For the M-L dimension, the dotted line indicates the midline. Genes are ranked from the most anterior to the most posterior based on their expression patterns in *Saccoglossus kowalevskii*. **e**, Spearman correlations between the ranking of the AP patterning related genes and their position along the three dimensions of the RNA tomography. The dots indicate the raw correlation values obtained by using the highest z-score as a readout of gene position along each dimension, and by ranking the AP patterning related genes following observations in *S. kowalevskii*. The boxplots indicate the distribution of correlation values when determining the gene position along each dimension probabilistically, and simultaneously shuffling the ranking of the AP patterning related genes for each group. The distribution of correlations for the M-L dimension is significantly higher than for the P-D and O-A dimensions (Two-sided Wilcoxon-rank test). Centre lines: median; box: interquartile range (IQR); whiskers: highest and lowest values at ± 1.5 × IQR. **f**, Relative contribution of each group of AP patterning related genes to the Spearman correlation between the ranking of the AP patterning related genes and their position along the three dimensions of the RNA tomography. Anterior gene groups drive the P-D and M-L correlations, while the Hox genes are the main drivers of the O-A correlation.

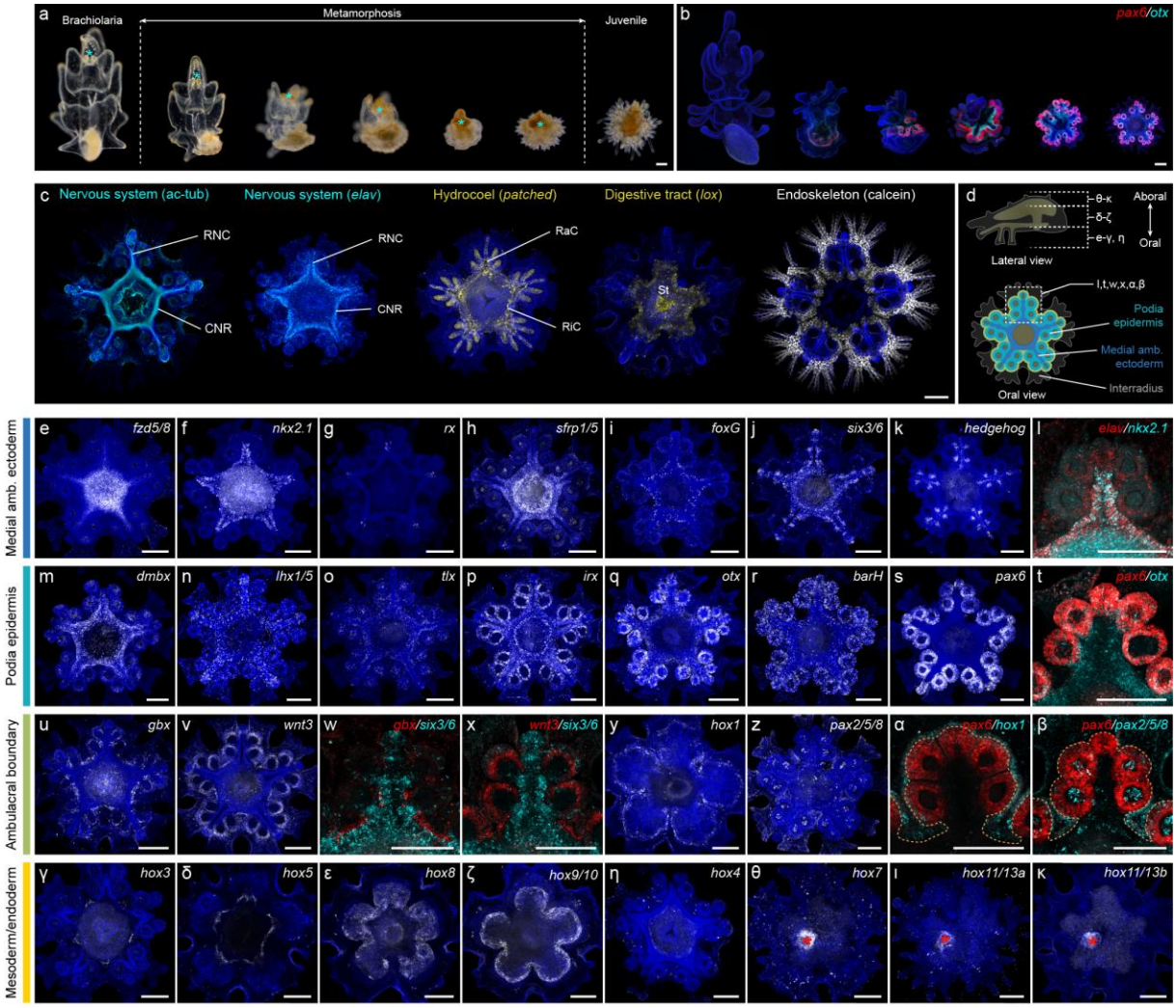

Figure 3: Gene expression data reveals the deployment of the antero-posterior patterning system in *Patiria miniata* ambulacral ectoderm

a, Metamorphosis in *P. miniata*. The anterior part of the brachiolaria larva (cyan asterisk) is resorbed into the rudiment. **b**, HCRs showing *pax6* (red) and *otx* (cyan) starting to be expressed during metamorphosis in the developing adult pentaradial body plan. Specimens are counterstained with DAPI (blue). **c**, Main anatomical features of post-metamorphic juveniles, imaged from the oral side: the nervous system (cyan) stained with antibodies against acetylated-tubulin highlighting the nerve tracts and the neuronal marker *elav* highlighting the cell bodies, the hydrocoel stained with the marker *patched*, the digestive tract stained with the marker *lox* and the endoskeleton stained using calcein. RNC: radial nerve cord; CNR: circumoral nerve ring; RaC: radial canal; RiC: ring canal; St: stomach **d**, Schematics showing the oral-aboral position of the HCR z-projections shown in **e-κ** (top) and the main anatomical regions visible on the post-metamorphic juveniles oral side (bottom). The white square on the bottom panel indicates the position of the close-ups in **l,t,w,x,α,β**. **e-κ**, HCRs of *P. miniata* juveniles imaged from the oral side (**e-η**) or the aboral side (**θ-κ**). In **e-k,m-s,u,v,y,z,γ-κ,** specimens are counterstained with DAPI (blue). **l,t,w,x,α,β,** magnification of a single ambulacrum. **e-l**, Genes primarily expressed in the medial ambulacral ectoderm. Colocalization with *elav* indicates expression in the CNR and the RNCs. **m-t**, Genes primarily expressed in the podia epidermis. **u-β**, Genes primarily expressed in the ambulacral boundary. In **α,β,** orange dotted lines outline the ambulacral ectoderm. **γ-ζ**, Hox genes primarily expressed in the coeloms. **η-κ**, Hox genes primarily expressed in the digestive tract. In **θ-κ,** red asterisks indicate the position of the developing intestinal tract. Scale bars = 100µm.

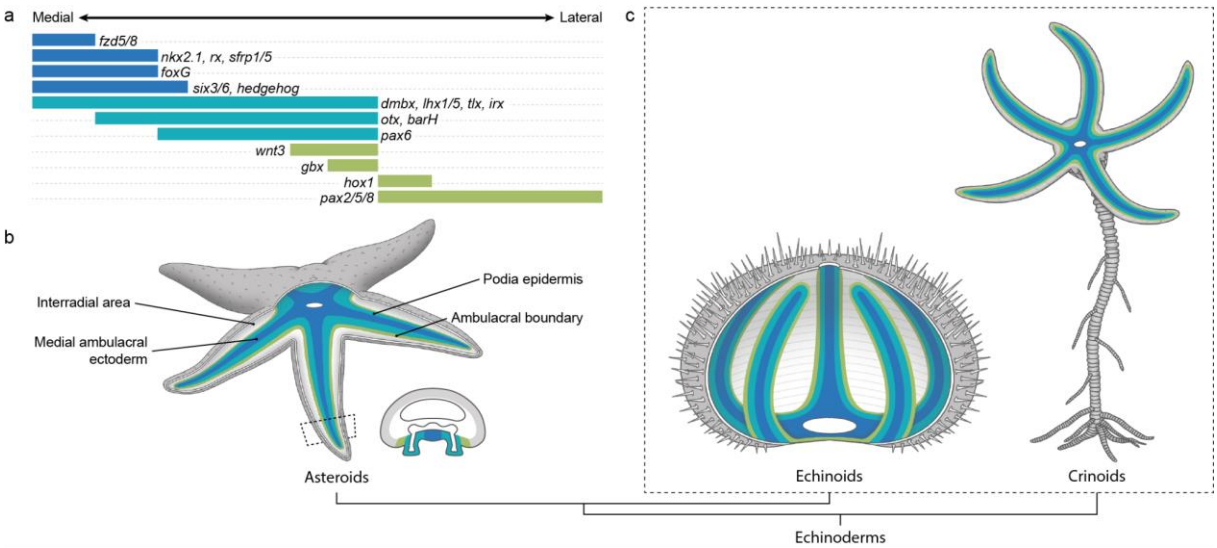

Figure 4: The ambulacral-anterior model of echinoderm body plan evolution

a, Expression map of the conserved transcription factors and signaling ligands involved in the ambulacral ectoderm patterning in *Patiria miniata*, organized from the midline of the ambulacrum (left) towards the interradius (right). **b**, Diagram of the ambulacral-anterior model in a generalized asteroid. Anterior patterning genes are expressed in the oral ambulacral ectoderm, shown through a cut-away of the forward part of the animal and a cross-section through the forward arm. Only genes expressed in the ectoderm are shown. **c,** Ambulacral-anterior model applied to echinoderm classes with available gene expression data, echinoids (left) and crinoids (right). In echinoids, the ambulacral ectoderm is internalized and shown through a cut-away of the forward part of the test, while in crinoids the ambulacral ectoderm is embedded in the oral epidermis, similar to asteroids.

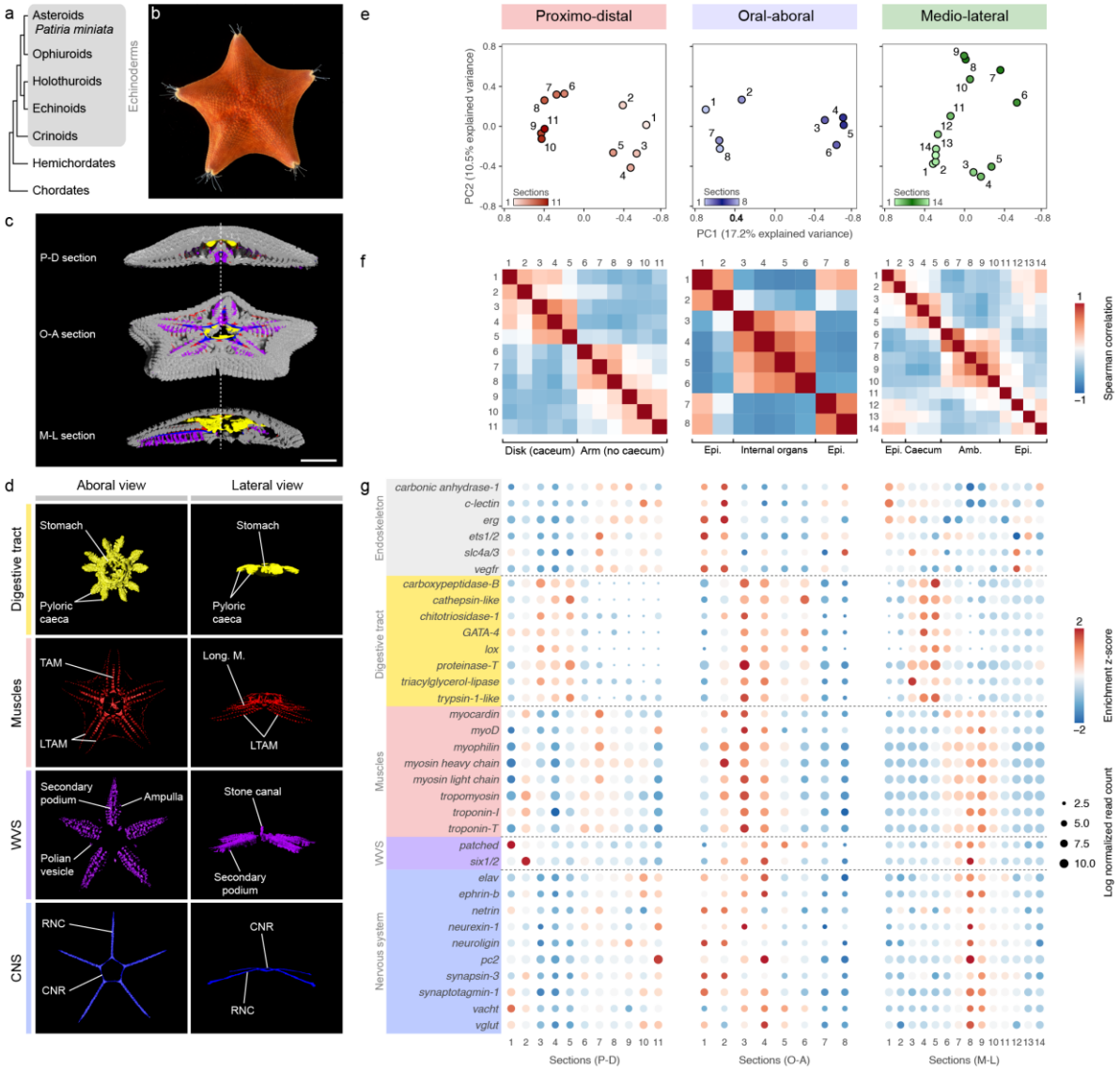

Extended Data Figure 1: *Patiria miniata* anatomy is reflected by RNA tomography

a, Phylogenetic position of *P. miniata* within deuterostomes, the grey box highlights the echinoderm phylum. **b**, Young adult *P. miniata*, viewed from the aboral side. **c,d,** Reconstructions of a young juvenile *P. miniata* scanned by micro-CT and segmented to highlight the main anatomical features of the animal, including the endoskeleton (grey), the digestive tract (yellow), the main body muscles (red), the water vascular system (WVS; purple) and the central nervous system (CNS; blue). **c,** Lateral views showing virtual sections of the micro-CT reconstruction along the proximo-distal (P-D), oral-aboral (O-A) and medio-lateral (M-L) dimensions used in the RNA tomography. Scale bar = 1mm. **d,** Details of the different anatomical features shown in aboral or lateral views. The different panels are shown at the same scale. TAM: transverse ambulacral muscle; LTAM: lateral transverse ambulacral muscle; Long. M: longitudinal muscle; RNC: radial nerve cord; CNR: circumoral nerve ring. **e,** Principal component analysis of the RNA tomography sections. For each dimension the sections are color-coded according to the geometry of the animal. **f,** Spearman correlations between the sections of the RNA tomography in each of the three dimensions. Epi: epidermis; Amb: ambulacrum. **g,** Expression profiles along the three dimensions of the RNA tomography for tissue marker genes known based on published literature to be expressed in the endoskeleton (grey), digestive tract (yellow), muscles (red), WVS (purple) and in the nervous system (blue) are consistent with the anatomy of the animal. Note that in the case of digestive tract markers, there is a left shift of expression in the L-R dimension that we assume resulted from displacement of the pyloric caeca during the dissection of the arm.

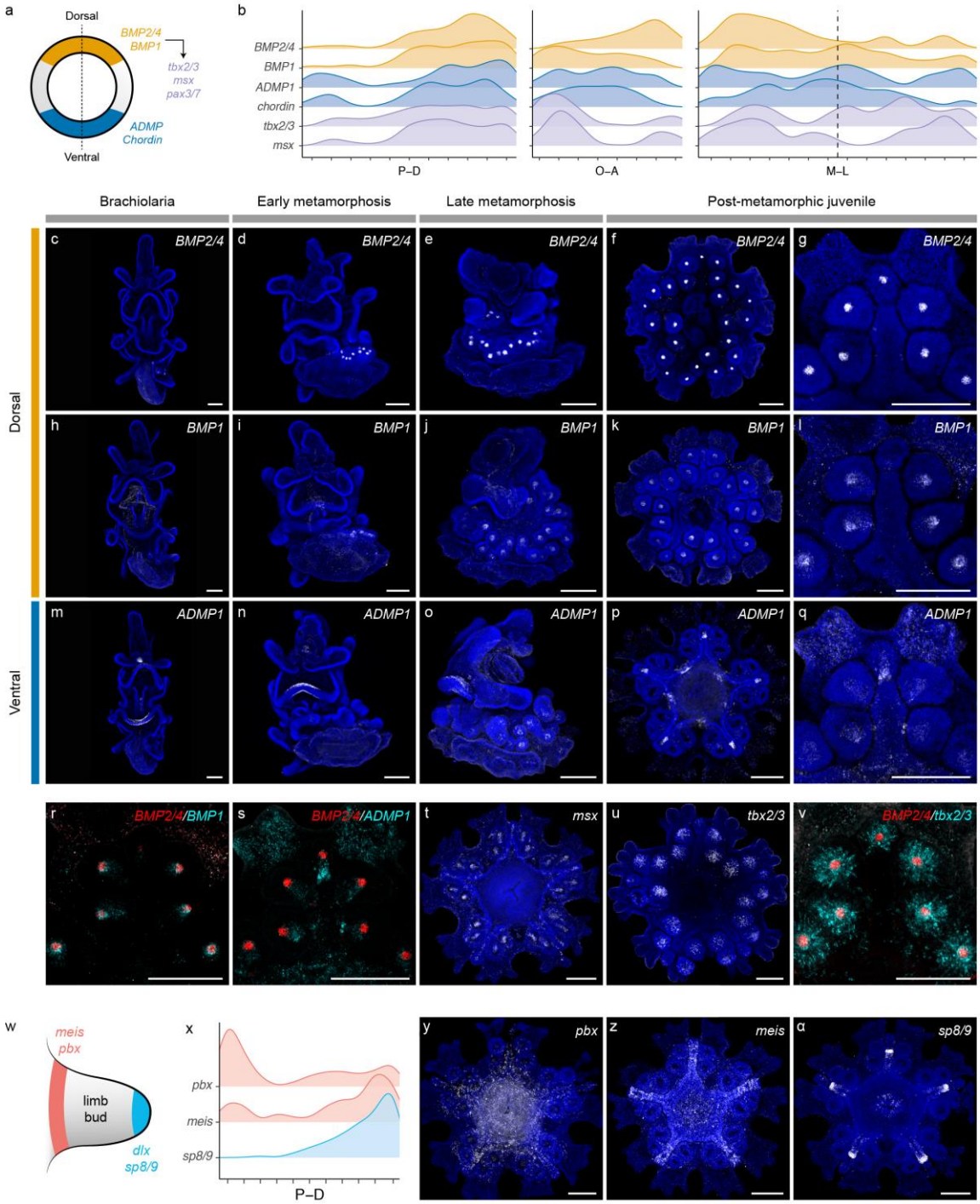

Extended Data Figure 2: Dorso-ventral and appendage patterning in *Patiria miniata*

a, Schematic representation of DV patterning in bilaterians. **b,** Expression profile of DV specification and patterning genes along the P-D, O-A and M-L dimensions of the RNA tomography. For the M-L dimension, the dotted line indicates the midline. **c-v,y-α,** HCRs of *P. miniata* brachiolaria (**c,h,m**), early metamorphosis (**d,i,n**), late metamorphosis (**e,j,o**) and post-metamorphic juveniles (**f,g,k,l,p-v, y-α**) imaged from the oral side. In **c-q,t,u,y-α,** specimens are counterstained with DAPI (blue). **g,l,q,r,s,v**, Magnification of a single ambulacrum. **c-v,** Expression patterns of genes involved in DV axis specification and patterning. **w,** Schematic representation of limb proximo-distal patterning in bilaterians. **x**, Expression profile of limb proximo-distal patterning genes along the P-D dimension of the RNA tomography. **y-α,** Expression patterns of genes involved in limb proximo-distal patterning. Scale bars = 100µm.